



# Computational Study of Combustor Dilution Flow Interaction with Turbine Vanes

Kirsten Muirhead\* and Stephen Lynch†

Pennsylvania State University, University Park, Pennsylvania 16802

DOI: 10.2514/1.B36912

Higher efficiency and greater performance in gas-turbine engines can be achieved by increasing the combustion temperature but is limited by durability concerns for downstream hardware. Large-scale dilution cooling flows can be injected in the combustor to promote mixing and reduce incoming temperatures, but this generates spatial and temporal nonuniformities for the first row of turbine vanes. The lack of uniformity is exacerbated as combustor designs are reduced in length to reduce overall engine weight, but little is known about how the vane surface conditions are affected. This work computationally modeled the flow in a previously studied nonreacting combustor simulator, using both time-average (steady Reynolds-averaged Navier–Stokes, RANS) and time-dependent (delayed detached-eddy simulation, DDES) analyses. The effect of several dilution hole configurations on the adiabatic wall temperature and heat transfer coefficient of the first vane were studied in the time-average approach. Configurations in which the dilution jets were closer to the vane resulted in some vane surface cooling but also significant flow nonuniformity at the turbine inlet, high vane temperature gradients, and increased heat flux to the vane. Heat transfer coefficient augmentation on the vane pressure side was more than three times higher than without upstream dilution, for dilution jets close to the vane. The time-dependent DDES analysis predicted a larger degree of mixing and more uniform vane temperatures, relative to the RANS analysis, but also indicated anisotropy of the turbulence entering the turbine, which cannot be correctly captured by a RANS approach. Refinement of the time-dependent analysis in a region around the dilution jets did not significantly change the turbine inlet flowfield and had only a minor impact on the predicted vane surface temperature. Overall, the results indicate that nonuniform flow in the combustor can significantly impact vane temperature but should be modeled using scale-resolving simulations for best accuracy.

## Nomenclature

$C$	= vane true chord, 59.4 cm
$C_p$	= nondimensional static pressure; $(P_s - \bar{P}_s)/(1/2\rho\bar{U}^2)$
$h$	= convective heat transfer coefficient, $W/(m \cdot K)$
$I$	= momentum flux ratio between jet and freestream; $\rho_c V_c^2 / \rho_\infty V_\infty^2$
$k$	= turbulent kinetic energy; $(1/2)(\overline{u'^2} + \overline{v'^2} + \overline{w'^2})$ , $m^2/s^2$
$L_k$	= estimated Kolmogorov scale, m
NHFR	= net heat flux reduction
$P$	= pressure, Pa
$\bar{P}_s$	= mass-average turbine inlet plane static pressure, Pa
$Pr_t$	= turbulent Prandtl number
$q''$	= wall heat flux, $W/m^2$
$S$	= vane span, 54.6 cm
$s$	= surface distance around the vane from the leading-edge stagnation, m
$T$	= temperature, K
$t$	= time, s
$U$	= time-average axial velocity, m/s
$\bar{U}$	= mass-average turbine inlet axial velocity (space- and time-average), m/s
$U_{in}$	= domain inlet velocity, m/s
$u$	= axial velocity ( $x$ direction), m/s
$V$	= magnitude of velocity, m/s
Vol	= volume of cell, $m^3$
$v$	= pitchwise velocity ( $y$ direction), m/s

$w$	= spanwise velocity ( $z$ direction), m/s
$X, Y, Z$	= global coordinates (axial, pitchwise, spanwise), m
$y^+$	= nondimensional wall distance based on wall shear; $y\sqrt{\tau_s/\rho\nu}$
$\alpha$	= molecular thermal diffusivity, $m^2/s$
$\epsilon$	= turbulence dissipation rate per unit mass, $m^2/s^3$
$\eta$	= nondimensional surface temperature; $(T_\infty - T_{aw})/(T_\infty - T_c)$
$\theta$	= nondimensional freestream temperature; $(T_\infty - T)/(T_\infty - T_c)$
$\mu_{SGS}$	= subgrid-scale turbulent viscosity, $(kg \cdot m)/s^2$
$\mu_t$	= turbulent viscosity, $(kg \cdot m)/s^2$
$\nu$	= kinematic viscosity, $m^2/s$
$\rho$	= density, $kg/m^3$
$\varphi$	= nondimensional metal temperature; $(T_\infty - T_w)/(T_\infty - T_c)$
$\omega$	= specific turbulence dissipation rat, 1/s

## Subscripts

aw	= adiabatic wall condition
$c$	= coolant condition
$i$	= Cartesian coordinate index
$s$	= surface (nonadiabatic) condition
$o$	= without dilution flow
$w$	= wall condition
$\infty$	= freestream condition
$\overline{(\ )}$	= rms of quantity

Presented as Paper 2017-0109 at the AIAA SciTech Conference, Grapevine, TX, 9–13 January 2017; received 14 September 2017; revision received 14 June 2018; accepted for publication 1 August 2018; published online 29 October 2018. Copyright © 2018 by Stephen Lynch. Published by the American Institute of Aeronautics and Astronautics, Inc., with permission. All requests for copying and permission to reprint should be submitted to CCC at www.copyright.com; employ the ISSN 0748-4658 (print) or 1533-3876 (online) to initiate your request. See also AIAA Rights and Permissions www.aiaa.org/randp.

\*Undergraduate Student, Aerospace Engineering Department; United Technologies—Pratt & Whitney, Member AIAA.

†Assistant Professor, Mechanical Engineering, Senior Member AIAA.

## I. Introduction

Increasing the combustion temperature and by decreasing the amount of uncombusted cooling air required to prevent component overheating. More effective component cooling with less coolant requires a more precise understanding of thermal loads on hot-section components. The first row of nozzle guide vanes downstream of the combustor are subjected to some of the highest heat loads in the engine. They are cooled with film cooling on the vane outer surfaces (small-scale coolant flows) as well as internal cooling through

interior channels. However, the amount of vane cooling required is highly dependent on the incoming conditions, including both the distribution of the temperature field as well as the turbulence of the flow.

In a typical aeroengine rich–quench–lean (RQL) style combustor, turbulent flow is desirable to provide adequate mixing for completion of combustion as well as for dilution of hot products. Dilution cooling is accomplished by injecting uncombusted air into the combustor through large holes in the casing. These jets-in-crossflow produce turbulent vortical structures in their wakes and within the jet itself (Fric and Roshko [1]). The turbulence mixes and homogenizes the combusted flow, but some turbulent structures propagate downstream.

In industry, combustor modeling has evolved to capture the important dynamical motions of the flow via turbulent scale-resolving methods. However, in the turbine design, the spatial and temporal variation of these structures are often neglected, and the turbine inlet condition is reduced to an area-average value or possibly a circumferentially averaged profile (Barringer et al. [2]). Flow through the turbine inlet plane is nonuniform not only in space but also in time, resulting in nonuniform, time-variant thermal loading on the vanes. These nonuniformities may be further exacerbated by the reduction of gas-turbine core size for next-generation ultrahigh-bypass-ratio engines (Epstein [3]), where the combustor may need to be even more compact (McKinney et al. [4]). Understanding these effects is important to optimize cooling, so that gains in propulsive efficiency from high bypass ratios are not offset by losses in engine thermodynamic efficiency due to increased cooling requirements.

This computational study examines the effect of dilution flow interaction with a downstream turbine vane, based on a simplified geometry studied experimentally by Vakil and Thole [5]. The effect of dilution hole location is investigated using a steady Reynolds-averaged Navier–Stokes (RANS) approach. The importance of a turbulent scale-resolving (delayed detached-eddy simulation, DDES) approach is investigated for the baseline experimental dilution configuration, and the impact of refining the DDES model is tested.

## II. Previous Studies

Several studies have compared the effects of dilution hole parameters on time-average combustor exit flowfields. Holdeman and Walker [6] studied the effects of momentum flux ratios, diameter ratios, density ratios, and downstream distance of injection on jet penetration and temperature profiles of a single row of jets. Momentum flux ratio and diameter ratio proved to be the dominant variables, with penetration and mixing increasing with increasing momentum ratio and increasing jet diameter. Holdeman et al. [7] studied the mixing length of opposed and offset rows of jets more representative of a gas-turbine combustor and found that opposed configurations were most effective in homogenizing the temperature field downstream. Stevens and Carrotte [8] studied the effects of equally spaced jets in an annulus and discovered that the counter-rotating vortex pair is randomly asymmetrical. The twisting temperature contours that result are responsible for pitchwise asymmetry of the temperature distribution. The counter-rotating vortex pair dominates the flowfield downstream of the dilution jets. Stevens and Carrotte [9] further investigated the effects of jets in crossflow and concluded that the flowfield varies randomly from one jet to another and causes each jet to have its own mixing characteristics. This is responsible for the irregularity of the temperature within the annulus.

Dai et al. [10] studied multiple jets in confined crossflow and compared the effectiveness of directly opposed and staggered configurations. In the near field, directly opposed jets have better initial mixing than staggered jets at their respective optimum conditions. However, properly spaced staggered jets form a different vortex pattern, and the temperature and velocity contours at the combustor exit are more uniform relative to opposed jets. The staggered jets produce a larger-length-scale counter-rotating vortex pair that increases mixing. Barringer et al. [2] measured exit profile

conditions with and without dilution flow in the low-speed recirculating wind tunnel combustor simulator modeled in this study. The results of the study invalidated the common assumptions of either a constant total pressure field or a turbulent boundary layer for vane inlet conditions and found that turbulent length scales exiting the combustor were on the order of the dilution jet diameter.

Some studies have investigated combustor flowfields in more detail. Vakil and Thole [5] measured thermal fields and mean and fluctuating velocities generated by the dilution jets in the same combustor simulator of Barringer et al. [2]. Kidney-shaped thermal fields were present, indicating the presence of counter-rotating vortex pairs. The directly opposed dilution jets in that study impacted one another, evidenced by the spreading of the kidney-shaped contours in the mainstream. A recent study by Cha et al. [11] examined the nozzle guide vane inlet plane using an annular combustor simulator. The study concluded that the turbine inlet is dominated by the upstream dilution jet dynamics, is highly turbulent, and is highly nonuniform with regard to temperature distribution. However, there were no measurements shown for the vane.

Computational modeling of combustor flowfields is now commonly done using high-fidelity methods such as large-eddy simulation (LES) or related variants (di Mare et al. [12], Moin and Apte [13], Patil and Tafti [14], Boudier et al. [15]), to capture the complex fluid dynamics and chemistry that occurs. Cha et al. [16] reported that time-averaged LES and RANS calculations of velocity and turbulence intensity at the combustor exit agree with experimental trends, with LES producing more accurate data than RANS. Peak turbulence intensities at the turbine inlet plane are approximately 35%, with turbulence generated mainly by the dilution jets.

However, high-fidelity computational fluid dynamics (CFD) has not yet become as common for the turbine, due to the much higher Reynolds numbers and compressibility effects that are computationally expensive to simulate. This has led to various coupling approaches to transfer information from the combustor to the turbine. A common form is to link two separate codes, optimized for their respective flow regimes. Salvadori et al. [17] proposed loosely coupled and decoupled approaches to merge the high-fidelity CFD model in a combustor with the RANS model typically used in a turbine. Insinna et al. [18] coupled separate RANS solvers for a swirl-stabilized combustor and a turbine, respectively, and validated the coupled solution using turbine vane surface pressures. A full-engine simulation was performed by Medic et al. [19], which linked compressible RANS solvers in the compressor and turbine with an LES solver in the combustor using a separate coupling code.

Another combustor–turbine coupling approach that is gaining popularity is to adapt the code to handle both the low-speed highly turbulent chemically reacting regime and the high-speed turbine regime simultaneously. Klapdor et al. [20] adapted a pressure-based scheme to handle both the low-speed combustor and high-speed turbine but used a RANS approach throughout to model the turbulence. Andreini et al. [21] used a relatively new partial scale-resolving approach called scale-adaptive simulation (SAS), which can enable LES-like behavior in regions with large-scale turbulent motions but reverts to unsteady RANS in regions with low instability. Comparison to a combustor–turbine sector rig indicated better prediction of the combustor exit flow and temperature field with SAS versus a steady RANS approach, although no vane was modeled in the study.

In the turbine, it is well known that high turbulence levels and nonuniform temperature profiles can affect vane heat transfer, although many studies intentionally consider uniform inlet velocity at the turbine inlet plane. A series of studies by Ames (Ames [22], Ames et al. [23], and Ames et al. [24]) found that the heat transfer at the stagnation and on the pressure side of the vane is heavily augmented by large-scale high-intensity turbulence. Radomsky and Thole [25] simulated combustor-relevant freestream turbulence levels of 20% and concluded that turbulence levels do not decay in the vane passage but rather remain elevated and continue to augment heat transfer along the entire surface of the vane. More sophisticated combustor–turbine simulators have come online recently (Barringer

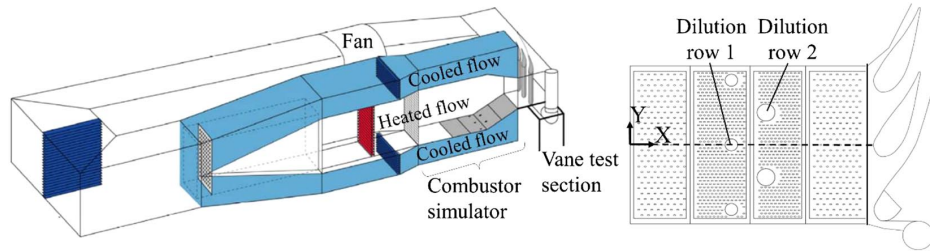


Fig. 1 Experimental combustor simulator geometry of Vakil and Thole [5], modeled in this study.

et al. [26], Povey and Qureshi [27], and Basol et al. [28]), underscoring the interest in capturing combustor–turbine interactions at higher fidelity, and yet vane surface quantities are not reported in much detail. A recent conjugate CFD study of a cooled vane by Griffini et al. [29] indicated some potentially severe impacts to cooling uniformity and vane temperature for realistic nonuniform turbine inlet conditions.

This study computationally replicates the nonreacting experimental study of Vakil and Thole [5], which has a simple combustor geometry and well-defined boundary and geometry conditions. For the purpose of validation of the study at hand, the effects of reacting flow are considered to be secondary relative to the significant flow disturbance of the dilution jets. A recognized limitation of this assumption is that there may be secondary reactions occurring in the shear layers of the coolant jet that could increase the temperature of the dilution flow; however, the large diameter of the dilution jets and the high momentum flux ratios studied here would still provide a significant amount of cold air. The unique aspects of this work are the consideration of a dilution jet flowfield on the spatially and temporally resolved turbine inlet condition and vane heat transfer as well as the effects of a wide range of dilution hole positions on vane cooling.

### III. Computational Setup

The combustor simulator of Vakil and Thole [5], modeled in this study, is shown in Fig. 1, including the large low-speed wind tunnel to which the simulator is attached. The tunnel has temperature conditioning heat exchangers and an electric heater upstream of the combustor simulator to generate temperature variation between core and dilution flow. The linear simulator is periodic in the pitchwise ( $Y$ ) direction, which enables a single vane to be modeled in this study, conserving computational resources. The combustor simulator has two rows of large dilution holes, with one hole in the first row and two half-holes in the second row (in a periodic mesh straddling the vane), and it is designed to simulate a typical aeroengine RQL combustor in both the convergence geometry and the fluid dynamic scaling (momentum flux ratios, dilution mass addition). For this study, no combustor liner effusion holes are modeled; these are not expected to have an impact on the dilution jet trajectory or the mixing in the midspan of the tunnel. The vane is based on an aeroengine first vane (Kang et al. [30]) and is located directly downstream of the combustor simulator. Dilution flow conditions for Vakil and Thole [5] are shown in Table 1.

The computational mesh of the combustor simulator and vane was generated in Pointwise. The computational domain is shown in Fig. 2. The periodicity in the experiment was exploited in the domain development. For all simulations in this study, the computational mesh was structured (hexahedral) in the vane boundary layer, with the first grid point from the vane surface at a  $y^+ \sim 1$  and an expansion

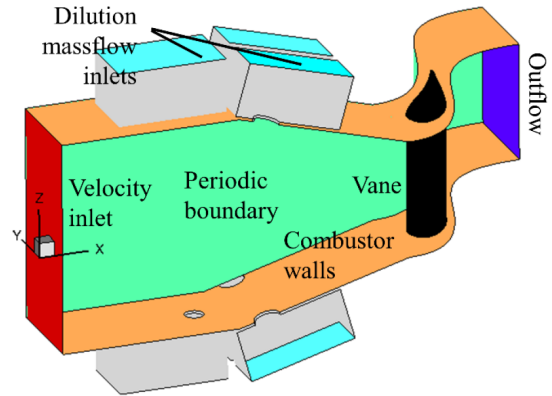


Fig. 2 Periodic model of combustor simulator, including supply plenums for dilution flow.

ratio of 1.3. Unstructured (tetrahedral) mesh was employed throughout the rest of the domain.

Boundary conditions for the model were set to the same conditions as the experiment, including the inlet velocity to the domain. Dilution plenums were constructed for each hole, to provide independent control over the dilution flowrates. Mass flow inlet boundary conditions were set on each of the dilution plenums, to the same conditions as the Vakil and Thole [5] study (see Table 1). All other surfaces were modeled as no-slip adiabatic walls.

The vane surface was modeled in two ways, with two separate simulations, to obtain both the adiabatic film temperature and heat transfer coefficients on the vane. The adiabatic film temperature  $T_{aw}$  was obtained by setting the vane surface to adiabatic, with coolant injected at the temperatures in the reference study. The vane surface temperature was nondimensionalized as an adiabatic film effectiveness  $\eta$  using the mainstream and coolant temperatures:

$$\eta = \frac{T_{\infty} - T_{aw}}{T_{\infty} - T_c} \quad (1)$$

To obtain heat transfer coefficients, the vane surface temperature was fixed at a constant value ( $T_s = 300$  K), different from the temperatures of the dilution or mainstream flows. Then, the heat transfer coefficient  $h$  was obtained by dividing the computed vane surface heat flux by the difference between the fixed vane surface temperature and the adiabatic wall temperature from the adiabatic study:

$$h = \frac{q_s''}{T_s - T_{aw}} \quad (2)$$

Table 1 Dilution flow conditions of Vakil and Thole [5], used in this study

Dilution	Mass flow addition based on local flow rate, %	Momentum flux ratio based on local mass-averaged velocity	Mass flux ratio based on local mass-averaged velocity	Density ratio based on upstream flow conditions	Ratio of mass-averaged velocity to domain inlet velocity
1	18.5	128	12	1.12	1
2	12.5	32	6	1.12	1.6

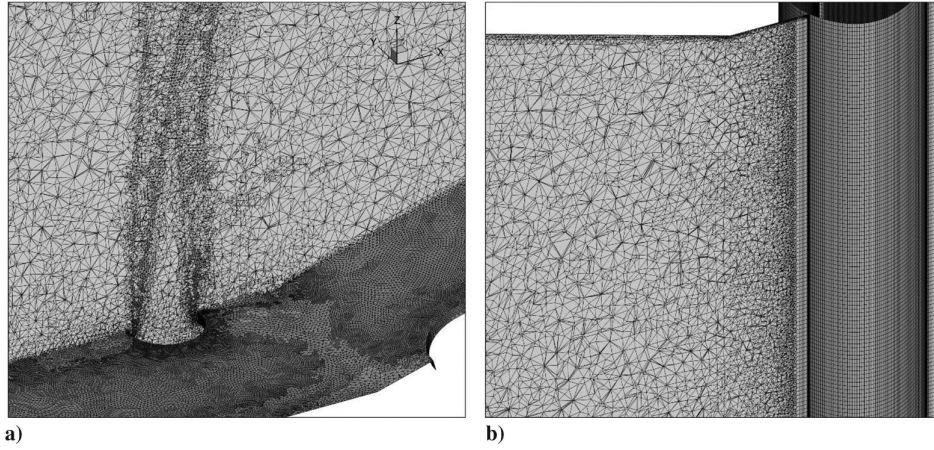


Fig. 3 Computational mesh after velocity gradient adaption at a) dilution centerline, and b) near the vane leading edge.

This was done to preserve the slight density variation between the coolant and mainstream so that both the momentum flux ratio and density ratio of the jets were the same between adiabatic vane and constant-temperature vane studies.

A third type of simulation was performed to generate a no-dilution case as a reference. The same physical combustor geometry and turbine inlet Reynolds number were maintained, but the dilution inlets were converted to walls to prevent dilution flow. The vane was given the same constant temperature, and the heat transfer coefficient for no dilution flow was determined by dividing the computed vane surface heat flux by the difference between the fixed vane surface temperature and the mainstream inlet temperature:

$$h_o = \frac{q_s''}{T_s - T_\infty} \quad (3)$$

The no-dilution case was used to normalize the heat transfer coefficients from the dilution flow cases. Note that this required the inlet velocity of this simulation to be adjusted so that the turbine inlet mass-average velocity (and thus turbine inlet Reynolds number) remained the same between the nondilution and dilution flow cases.

Properties for air were as follows: density was calculated with the incompressible ideal gas law, temperature dependence of molecular viscosity was modeled by Sutherland's law, specific heat was constant at 1006.43 J/(kg · K), thermal conductivity was constant at 0.0242 W/(m · K), and molecular weight was 28.933 kg/kmol. Reference values for the simulation were a domain inlet velocity of  $U_{in} = 1.93$  m/s, domain inlet temperature of  $T_\infty = 332.19$  K, and a coolant inlet temperature of  $T_c = 295.7$  K, in accordance with the boundary conditions of Vakil and Thole [5].

The solution-based grid adaption feature in ANSYS Fluent was used to refine the mesh locally in regions of high gradients, such as the jet shear layers shown in Fig. 3a, to improve resolution and study grid convergence. The computational meshes of the original configuration were refined by velocity gradient to increase grid size by 10% of total cell count of the previous mesh. Figure 4 shows the percent difference between mass-averaged quantities of turbine inlet velocity magnitude and area-averaged vane surface temperature from the adiabatic cases. The difference between the smallest mesh size (61% of largest mesh size) and the largest mesh size was less than 1%. The grid size used for all RANS cases in this study was 17.9 million cells (90% of largest mesh size).

#### A. Steady Reynolds-Averaged Navier–Stokes Simulations

An initial study of the effect of dilution hole position on turbine inlet flow uniformity and vane surface temperature was done using a steady Reynolds-averaged Navier–Stokes (RANS) approach. The steady incompressible Navier–Stokes equations in Reynolds-averaged form are given here in Cartesian tensor format, where the index ranges from 1 to 3; 1 corresponds to the  $x$  direction, 2 to the  $y$

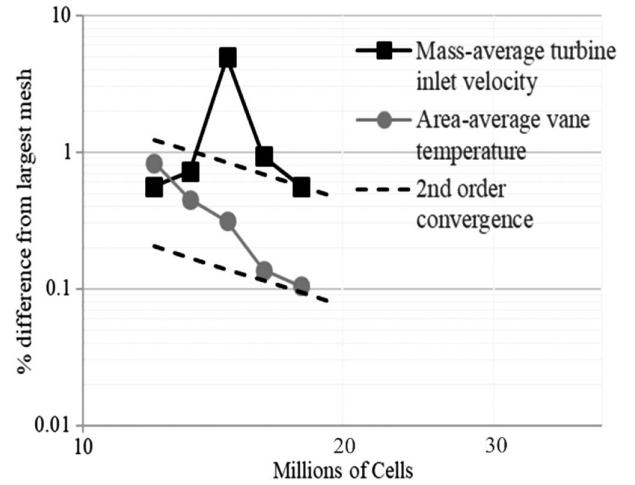


Fig. 4 Grid refinement study, with percent difference from the largest mesh (19 million cells).

direction, and 3 to the  $z$  direction. The modeled mass, momentum, and energy conservation equations are

$$\frac{\partial U_i}{\partial x_i} = 0 \quad (4)$$

$$U_j \frac{\partial U_i}{\partial x_j} = -\frac{1}{\rho} \frac{\partial P}{\partial x_i} + \frac{\partial}{\partial x_j} \left[ \nu \left( \frac{\partial U_i}{\partial x_j} + \frac{\partial U_j}{\partial x_i} \right) - \overline{u'_i u'_j} \right] \quad (5)$$

$$U_j \frac{\partial T}{\partial x_j} = \frac{\partial}{\partial x_j} \left[ \alpha \frac{\partial T}{\partial x_j} - \overline{u'_j T'} \right] \quad (6)$$

The shear-stress transport (SST)  $k - \omega$  model by Menter [31] was employed to close the RANS equations, using the Boussinesq approximation for the Reynolds stress and turbulent heat flux terms:

$$-\overline{u'_i u'_j} = \frac{\mu_t}{\rho} \left( \frac{\partial U_i}{\partial x_j} + \frac{\partial U_j}{\partial x_i} \right) - \frac{2}{3} k \delta_{ij} \quad (7)$$

$$-\overline{u'_j T'} = \frac{\mu_t}{\rho Pr_t} \frac{\partial T}{\partial x_j} \quad (8)$$

The turbulent viscosity  $\mu_t$  is determined by solving additional conservation equations for the turbulent kinetic energy  $k$  and specific dissipation rate  $\omega$ :

$$U_j \frac{\partial k}{\partial x_j} = \frac{\partial}{\partial x_j} \left[ \left( \nu + \frac{\mu_t}{\rho \sigma_k} \right) \frac{\partial k}{\partial x_j} \right] + [2\mu_t S_{ij} S_{ij}] - [(\beta^*) f_{\beta^*} k \omega] \quad (9)$$

$$U_j \frac{\partial \omega}{\partial x_j} = \frac{\partial}{\partial x_j} \left[ \left( \nu + \frac{\mu_t}{\rho \sigma_\omega} \right) \frac{\partial \omega}{\partial x_j} \right] + \left[ \frac{\alpha}{\mu_t} (2\mu_t S_{ij} S_{ij}) \right] - [\beta_t \omega^2] \\ + \left[ 2(1 - F_1) \frac{1}{\omega \sigma_{\omega,2}} \frac{\partial k}{\partial x_j} \frac{\partial \omega}{\partial x_j} \right] \quad (10)$$

The terms in the square brackets on the right side of Eq. (9) are the diffusion, production, and dissipation of turbulent kinetic energy, respectively. The square bracketed terms on the right of Eq. (10) are the diffusion, production, dissipation, and the cross-diffusion (resulting from the blending of the  $k - \epsilon$  and  $k - \omega$  models; see Menter [31]) of the specific dissipation rate, respectively. The turbulent viscosity is defined as

$$\mu_t = \frac{\rho k}{\omega} \frac{1}{\max[(1/\alpha^*), (SF_2/a_1 \omega)]} \quad (11)$$

All model constants and blending functions in Eqs. (9) and (10) (see Menter [31,32]) are the standard values and formulations as implemented in Fluent, and the turbulent Prandtl number was fixed at the recommended value of 0.85.

The pressure-based formulation of the preceding equations was employed, with second-order spatial discretization and upwinding for convective terms. The SIMPLE pressure-velocity coupling scheme was used in the solution. The steady simulations were generally run for at least 12,000 iterations or longer and declared converged when residuals were less than  $10^{-4}$  (energy less than  $10^{-6}$ ) and were unchanging for at least 200 iterations. Several other checks were also performed to determine convergence of the solution, including monitoring the area average pressure and temperature at the turbine inlet plane to confirm that it did not change by more than 1% over 500 iterations.

In all, five dilution hole configurations were studied, as shown in Fig. 5. The baseline configuration based on Vakil and Thole [5] had dilution jets that were directly in-line with each other on the top and bottom walls of the simulator (referred to as directly opposed). Two

other directly opposed cases were analyzed: a shift of the baseline pattern toward the vanes by 50% of the streamwise distance to the vane (referred to as short mixing length), and a case with a dilution pattern that was shifted both in the streamwise direction (short mixing length) and in the pitchwise direction by 50% of the domain width, simulating clocking of the vane relative to the dilution pattern.

Two other cases were studied where the upper and lower dilution hole patterns were offset from each other by 50% of the domain width, which is more typical of combustor dilution designs. For these offset cases, one was the original configuration (long mixing length) offset with a 50% pitchwise shift, and the other was that same pattern shifted streamwise (short mixing length). The combination of cases investigates the effect of directly opposed versus offset dilution hole patterns, as well as the effect of streamwise mixing length, on the uniformity of the flow entering the turbine. The streamwise shift of the dilution pattern toward the vanes is not necessarily based on an industry trend or consideration of existing technology; however, there is constantly a desire to reduce overall engine weight as much as possible, and reduction in combustor length has multiple benefits, including both material reduction in the combustor as well as reduction of the shaft length between the turbine and compressor. Furthermore, this does appear to be a design consideration for modern RQL combustors (McKinney et al. [4]). In this study, the close proximity of the holes to the vane inlet for the short-mixing-length cases likely provides an upper bound for turbulence levels in a dilution scheme of this type.

## B. Time-Resolved Simulations

Time-variant simulations of the baseline model were also examined in this study using the delayed detached-eddy simulation (DDES) model available in Fluent [32,33]. This method resolves turbulent structures in the main flowfield and models turbulence near the wall using unsteady RANS with the aforementioned SST  $k - \omega$  turbulence model. DDES was deemed more practical for this flowfield than a full LES simulation because of the reduced resolution requirements and because the details of the boundary layer were of less interest than the evolution of the turbulent structures in the main flowfield.

The mathematical formulation of the DDES approach is a hybrid between large-eddy simulation (LES) and RANS. LES relies on a low-pass filtering operation for the Navier–Stokes equations, so that large low-frequency energetic eddies are exactly determined, and higher-frequency small eddies are modeled. In ANSYS Fluent, the filter is based on the finite volume discretization of the domain; that is, eddies smaller than a computational cell are filtered, but their effect is represented by a subgrid-scale stress term (or enthalpy flux term, for enthalpy transport). For regions near walls, where turbulent eddies naturally have a smaller scale, the DDES approach instead employs unsteady RANS to close the conservation equations, to avoid the need for increasingly small cell volumes. The filtered mass, momentum, and energy conservation equations for incompressible flow of a calorically perfect gas are nearly identical to Eqs. (4–6) but are repeated next:

$$\frac{\partial U_i}{\partial x_i} = 0 \quad (12)$$

$$\frac{\partial U_i}{\partial t} + U_j \frac{\partial U_i}{\partial x_j} = -\frac{1}{\rho} \frac{\partial P}{\partial x_i} + \frac{\partial}{\partial x_j} \left[ \nu \left( \frac{\partial U_i}{\partial x_j} + \frac{\partial U_j}{\partial x_i} \right) - \overline{u_i' u_j'} \right] \quad (13)$$

$$\frac{\partial T}{\partial t} + U_j \frac{\partial T}{\partial x_j} = \frac{\partial}{\partial x_j} \left[ \alpha \frac{\partial T}{\partial x_j} - \overline{u_j' T'} \right] \quad (14)$$

Note here, however, that there are unsteady terms ( $\partial/\partial t$ ), and the last terms in the square brackets on the right sides of Eqs. (13) and (14) are the filtered subgrid-scale stress and enthalpy flux, respectively. In the DDES approach chosen here, the determination of the subgrid-scale quantities is based on the SST  $k - \omega$  turbulence model (Gritskevich et al. [33]), except the turbulent dissipation term

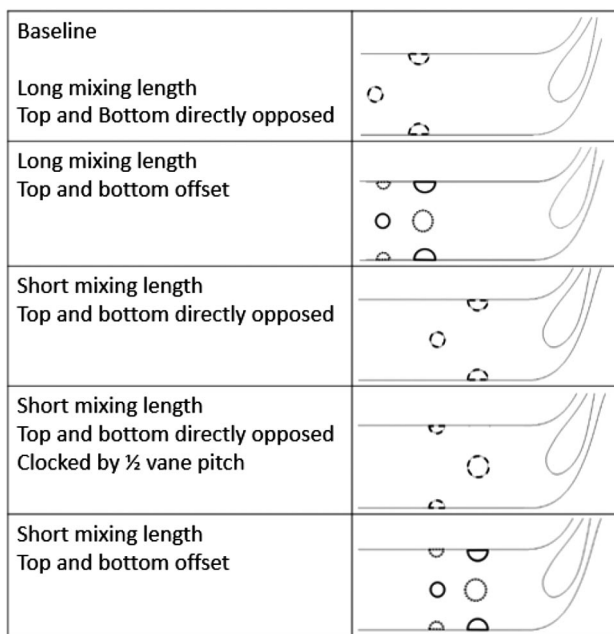


Fig. 5 Dilution configurations for steady RANS cases.

in the  $k$  equation is slightly modified:

$$U_j \frac{\partial k}{\partial x_j} = \frac{\partial}{\partial x_j} \left[ \left( \nu + \frac{\mu_{\text{SGS}}}{\rho \sigma_k} \right) \frac{\partial k}{\partial x_j} \right] + [2\mu_{\text{SGS}} S_{ij} S_{ij}] - [(\beta^*) k \omega F_{\text{DES}}] \quad (15)$$

The  $F_{\text{DES}}$  variable in the turbulent dissipation term [last bracketed term in Eq. (15)] acts as a limiter for the turbulent dissipation in regions that can be modeled using the LES approach and is represented as

$$F_{\text{DES}} = \max \left[ \left( \frac{\sqrt{k}}{\beta^* \omega} \right) \frac{1}{C_{\text{des}} \Delta_{\text{max}}} (1 - F_{\text{SST}}), 1 \right] \quad (16)$$

where  $F_{\text{SST}}$  is the zonal blending function of the SST  $k - \omega$  model (Menter [31]). This formulation forces the model to follow a RANS approach near walls (delays the switch to the LES model). All model constants were kept to the default values.

The subgrid-scale viscosity is determined in exactly the same manner as for the SST  $k - \omega$  turbulence model [Eq. (11)]. It is used with the gradient hypothesis model [Eq. (7)] to close the momentum equation, and the energy equation is closed using the gradient hypothesis model [Eq. (8)] for the subgrid-scale enthalpy flux, which includes the subgrid-scale viscosity and a subgrid-scale Prandtl number of 0.85.

The geometric model for the DDES simulations was identical to that shown in Fig. 2, with the same boundary conditions and dilution configuration as the baseline RANS study. Two mesh sizes were examined, with a nominal mesh of 12 million cells based on grid refinements from a RANS study and a refined mesh with 25 million cells. To obtain the refined DDES mesh, the turbulent dissipation from a baseline RANS model was used to estimate the Kolmogorov length scale per Eq. (4), and the adaption tools in Fluent were used to split cells with a ratio of cell size (estimated as cube root of cell volume  $V$ ) to Kolmogorov length scale  $> 100$  (Agarwal et al. [34]):

$$L_k = \left( \frac{\nu^3}{\varepsilon} \right)^{1/4} \quad (17)$$

Figure 6 shows a centerline slice through the combustor, with contours of the ratio of cell size to estimated Kolmogorov scale, for the nominal and refined DDES grids. The refinement was primarily in the dilution zone, and for these time-resolved cases with a more accurate prediction of turbulent dissipation, a cell size/Kolmogorov ratio below 100 was mostly achieved for the refined DDES, with some regions near the dilution jets that could still be refined.

The DDES simulations used a production limiter option available in Fluent and default model constants for the RANS part of the model. For the nominal mesh size of 12 million cells, a time step of  $2 \times 10^{-4}$  s was employed, so that the maximum convective Courant number was approximately 1. Unsteady simulations were run for five flow-through times in the domain (approximately 0.6 s for a single flow-through time) before sampling to ensure a statistically stationary flow. Monitors of velocity and temperature were employed throughout the flowfield to check statistical stationarity. After the simulation was determined to be statistically stationary, flow samples were collected for nine flow-through times. Figure 7 shows a comparison of the mean and rms of streamwise velocity at the turbine inlet plane, at the end of the eighth flow-through time versus the end of the ninth flow-through time. Only minor differences are noted between the results, suggesting temporally converged statistics.

The refined DDES simulation required a time step of  $1.2 \times 10^{-4}$  s to achieve a maximum convective Courant number of 1. Because of computing resource limitations, only two flow-through times were computed before beginning statistical sampling, and the total sample time was five flow-through times. All other model constants and boundary conditions were identical to the nominal DDES case.

#### IV. Comparison to Other Studies

The predicted vane static pressure distribution at midspan for the no-dilution case is presented as vane local inviscid velocity normalized by mass-averaged turbine plane inlet velocity in Fig. 8.

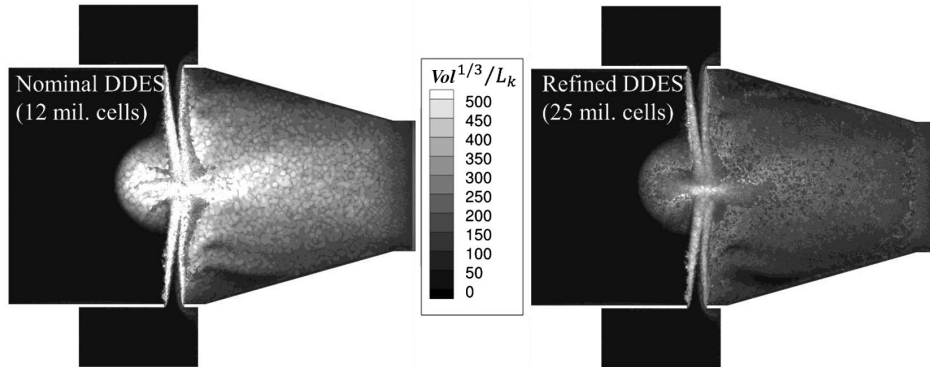


Fig. 6 Ratio of cell size to Kolmogorov length scale at an instant in time, for nominal DDES (left) and refined DDES (right).

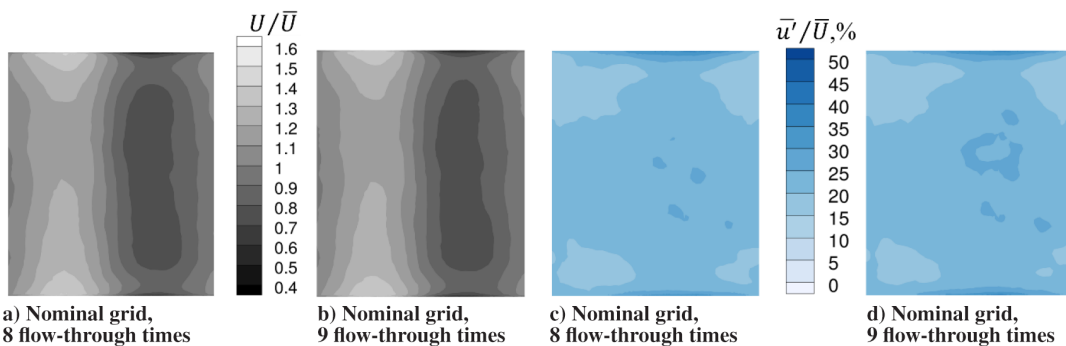


Fig. 7 Mean (Figs. 7a and 7b) and rms (Figs. 7c and 7d) of streamwise velocity at the turbine inlet plane for flow sampling over eight versus nine flow-through times, for the nominal grid DDES case.

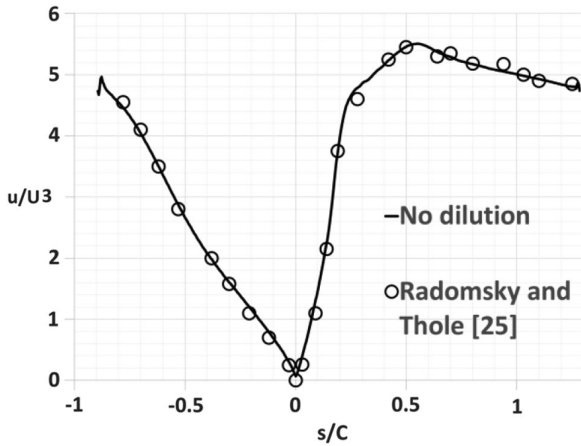


Fig. 8 Vane midspan inviscid velocity comparison.

The result compares very well to measurements by Radomsky and Thole [25] for the same vane, although their study had a uniform inlet area (no convergence). Vakil and Thole [5] did not measure vane surface quantities but set the combustor outlet to nominally the same vane inlet Reynolds number as Radomsky and Thole [25], and so the midspan vane flowfield without dilution was expected to be consistent.

The study by Vakil and Thole [5] modeled both dilution and combustor liner film cooling effects. The effects of film cooling are disregarded in this study because dilution flow dominates in the main gas path flowfield, and a majority of the coolant mass flow is supplied to the dilution holes. Figure 9 compares the predicted temperature field of the first-row dilution jet (on a plane passing through the center

of the jet) for the steady RANS, the time-average of the nominal DDES, and the experimental results of Vakil and Thole [5]. The prediction of the jet trajectory using a correlation by Lefebvre and Ballal [35] is overlaid on each case. The DDES case follows the correlation trajectory almost exactly, with the steady RANS jet also well-approximated by the correlation. These stand in sharp contrast to the experimental measurements, which show the jet being bent significantly by the main flowfield and penetrating to a lower span height. The reason for the discrepancy is not clear; several checks were performed to compare the total mass addition as well as the local momentum flux of the dilution jets to the values reported in Vakil and Thole [5], which all agreed. Simulations performed using a reduced dilution mass flow resulted in a closer match to the experimental jet behavior. Dilution jets with 25% of the reported experimental mass flow (not shown) are the closest qualitative match to the experimentally reported jet penetration and entrainment.

A prior computational study by Stitzel and Thole [36] of the same combustor simulator used by Vakil and Thole [5] produced results with similar trends to the current computational study. As seen in Fig. 10, the computation by Stitzel and Thole [36], which used steady RANS with an Renormalization Group (RNG)  $k-\epsilon$  turbulence model and symmetry planes at the combustor midspan, also shows strong jet penetration and a large recirculation region upstream of the first row of dilution holes. Note that the streamlines for the cases from this study are not enforced to be symmetric, and the steady RANS computations exhibited sensitivity to small mispredictions of the dilution jet trajectories.

## V. Results

This section first describes the impact of dilution hole location on the turbine inlet flow uniformity and vane surface heat transfer using steady RANS simulations. Then, the RANS solution for the baseline

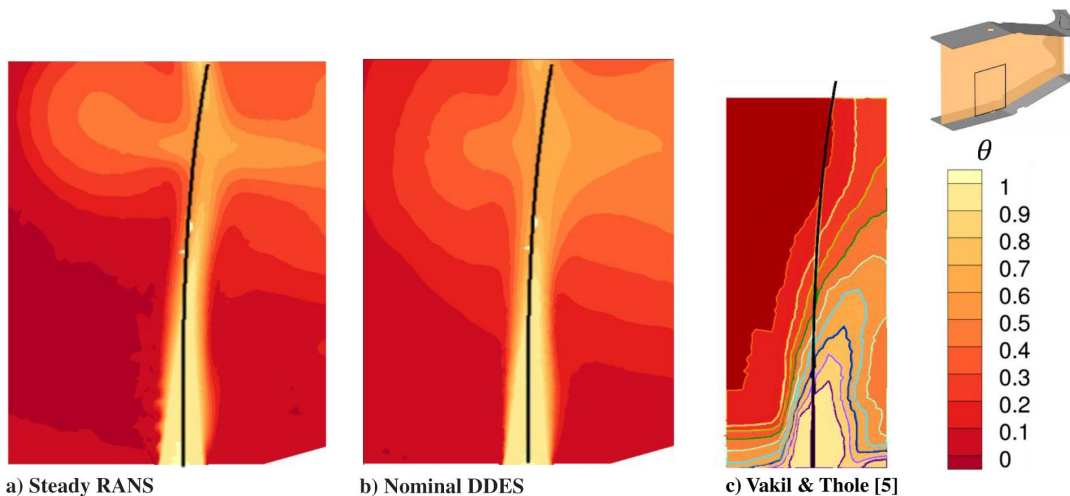


Fig. 9 Dilution centerline temperature, with a correlation for jet trajectory (line) by Lefebvre and Ballal [35] for a) steady RANS, b) time average of DDES, and c) experiment of Vakil and Thole [5].

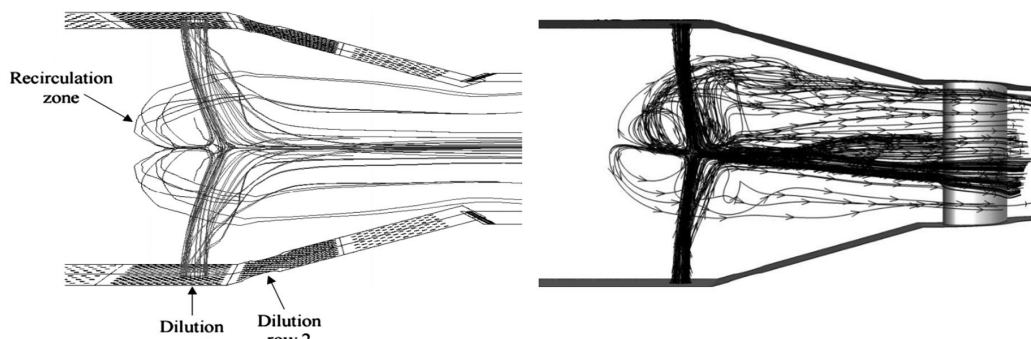


Fig. 10 Comparison of dilution hole streamlines for Stitzel and Thole [36] (left) and this study (right).

configuration is compared to a DDES calculation on the nominal grid size. Finally, the effect of grid refinement on the DDES solution result is investigated.

### A. Effect of Dilution Hole Location

Figure 11 shows the steady RANS predictions of the effect of dilution hole location on the nondimensional surface temperature of the combustor walls and the turbine vane. Iso-surfaces of nondimensional fluid temperature at  $\theta = 0.55$  are also shown, to indicate the trajectory of the dilution jets. Note that the surface nondimensional temperature  $\eta$  and the fluid nondimensional temperature  $\theta$  have identical definitions. A recognized limitation of

this study is the lack of reacting flow physics that might impact the flow and temperature fields around the dilution. In particular, there could be secondary reactions occurring in the high-turbulence regions of the dilution jets, such that the average temperature around the jet is increased. Recent studies of isolated reacting jets show chemiluminescence (indicative of reactions) up to two jet diameters (Wagner et al. [37]) or even 10 diameters downstream (Sullivan et al. [38]). This could result in higher local temperatures at the turbine inlet plane than indicated in this study and should be considered in future work.

For the baseline case with directly opposed jets, the RANS model predicts very strong jet penetration ( $I = 128$  for the first row), with

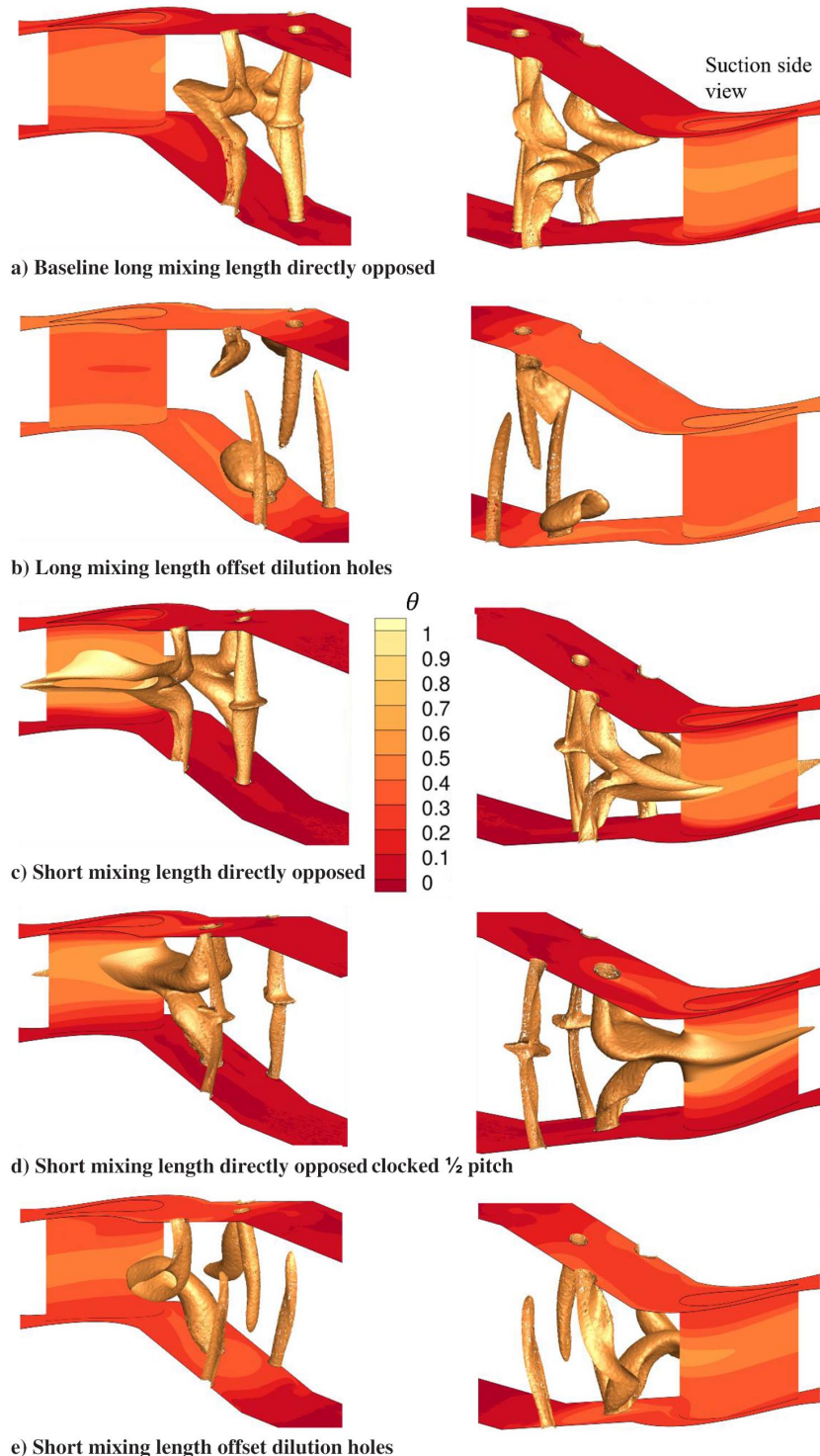


Fig. 11 Nondimensional surface temperature, and isosurface of  $\theta = 0.55$ , for the dilution hole positions.

jets that impact each other in the midspan of the combustor. Because most of the cooling flow interacts at the midspan, there is little to no coolant on the combustor wall or the turbine endwall surfaces (recall liner effusion cooling is not modeled in this study). However, the RANS model predicts a distinct band of cooler fluid on the vane at its centerline. This coolant distribution is not ideal for turbine durability due to both the hot zones near the endwalls as well as temperature gradients between the endwall and center that would cause differential thermal expansion and cracking issues.

The opposed jet configuration with the long mixing length in Fig. 11b shows very little interaction between jets in a given row, but there appears to be a significant interaction between the first-row jet and a second-row jet, whereby the second-row jet at a lower effective momentum flux ( $I = 32$ ) is pressed down toward the wall. Because of this, the combustor wall and turbine endwall temperatures are cooler than in the baseline case, but the vane airfoil midspan temperature is warmer.

The remainder of the cases in Fig. 11 are for the short mixing length, where the dilution pattern is shifted toward the turbine vane by 50% of the distance to the vane. In the directly opposed case with the short mixing length, the second-row dilution jets are predicted to impact directly on the vane pressure side and provide a significant amount of cooling. This may be a possible advantage in a short combustor design, whereby airfoil cooling could be reduced because of the dilution cooling. When the dilution pattern is clocked by half of a vane pitch, the large second-row dilution hole directly impacts the vane leading edge, causing even more cooling on the airfoil surface. However, all of the directly opposed cases for this short mixing length result in little to no cooling on the combustor walls or turbine endwalls, which creates severe temperature gradients in the vane. It is likely that there would need to be some significant cooling present for those surfaces (as is typical in current aeroengines, although not modeled here).

Finally, the effect of a short mixing length with an offset dilution hole pattern is seen in Fig. 11e. As for the long mixing length, an offset dilution hole pattern results in strong jet penetration for the first row. Unlike for the long mixing length, the second-row dilution jets in the short mixing length pattern are not suppressed by upstream jets and penetrate into the mainstream. This results in better mixing and more uniform distribution of wall temperatures on the airfoil and endwall surfaces, relative to the directly opposed configurations for the short mixing length.

Because of the flow disturbance of the dilution jets, especially for the short-mixing-length cases, it is possible that the local static pressure at the vane surface could be altered, which would impact local film coolant ejection (not modeled in this study). To examine the potential impact, Fig. 12 shows the nondimensional static pressure on the vane, referenced to the mass-average vane inlet plane static pressure and normalized by the mass-average vane inlet dynamic pressure resulting in a nondimensional pressure coefficient. Only the baseline case is shown for a long mixing length because differences

between the two long-mixing-length cases were insignificant, and only two of the short-mixing-length cases are shown, which had the most extreme variation. Figure 12 indicates a slight localized increase in static pressure ( $C_p$  values above 2) near the vane leading edge for the short-mixing-length cases, where the dilution jets are impacting the vane. The local pressure increase for the short-mixing-length cases relative to the baseline is about 1.4% of the typical total pressure at the vane inlet, assuming an engine overall pressure ratio of 40, a turbine inlet temperature of 2100 K, and a vane inlet Mach number of 0.15. This could be an issue for the leading-edge cooling on the first vane, given that the coolant backpressure margin (percent increase in coolant supply pressure relative to local gas path pressure) is typically less than 10%.

Figure 13 shows a comparison of normalized heat transfer coefficients on the vane surface for each configuration. The normalization was done by computing the vane surface heat transfer coefficient in the absence of dilution flow ( $h_0$ ), but with the exact same combustor convergence geometry as described earlier. The jagged striping in the contours is a result of near-wall streaks that were predicted in the no-dilution case. The origin of the streaks was unclear (the vane  $y^+$  was sufficiently low for the SST  $k - \omega$  model, and the incoming flow was uniform and smooth) but may be related to Görtler vortex features that are partially resolved by the turbulence model (Winoto and Crane [39]).

It is clear from Fig. 13 that the majority of the impact of turbulent dilution flow on vane surface heat transfer is on the pressure side of the vane. Furthermore, for a given flow mixing length, the offset configuration results in lower heat transfer near the vane midspan than the directly opposed cases. Also, for a given dilution configuration, the heat transfer is nominally higher for a short mixing length versus the long mixing length. The highest surface heat transfer is from the case with a short mixing length and the second-row dilution jet directly impinging on the vane pressure side. This suggests that this configuration may not in fact be the best for vane surface cooling, as seemed to be the case in Fig. 11e.

Because both the adiabatic cooling effectiveness and heat transfer coefficient ratio were calculated, it is possible to compute a net heat flux reduction parameter (Sen et al. [40]), which indicates the potential reduction (or increase) in convective heat flux to the part for a cooling scheme. Net heat flux reduction is given as

$$\text{NHFR} = 1 - \frac{q''}{q_0''} = 1 - \frac{h}{h_0}(1 - \eta\varphi) \quad (18)$$

where  $\varphi$  is a nondimensional metal wall temperature:

$$\varphi = \frac{T_\infty - T_c}{T_\infty - T_w} \quad (19)$$

In this analysis,  $\varphi$  is assumed to be 1.6 per the recommendation of Sen et al. [40]. Figure 14 shows NHFR on the pressure side of the

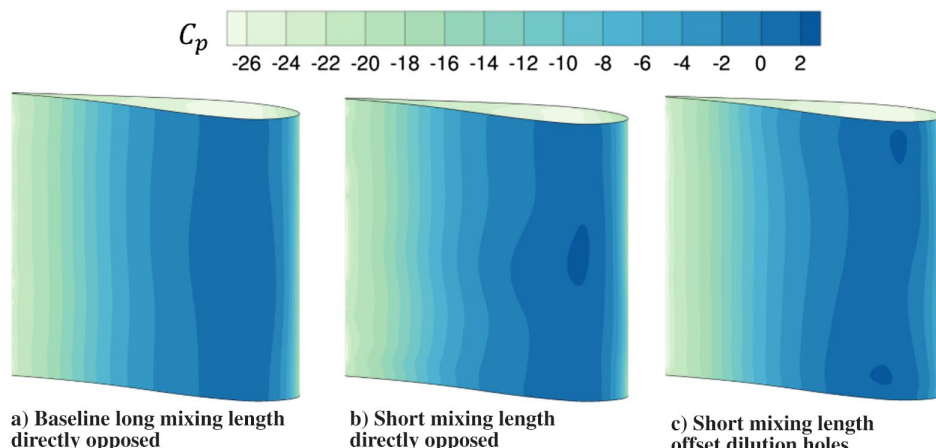
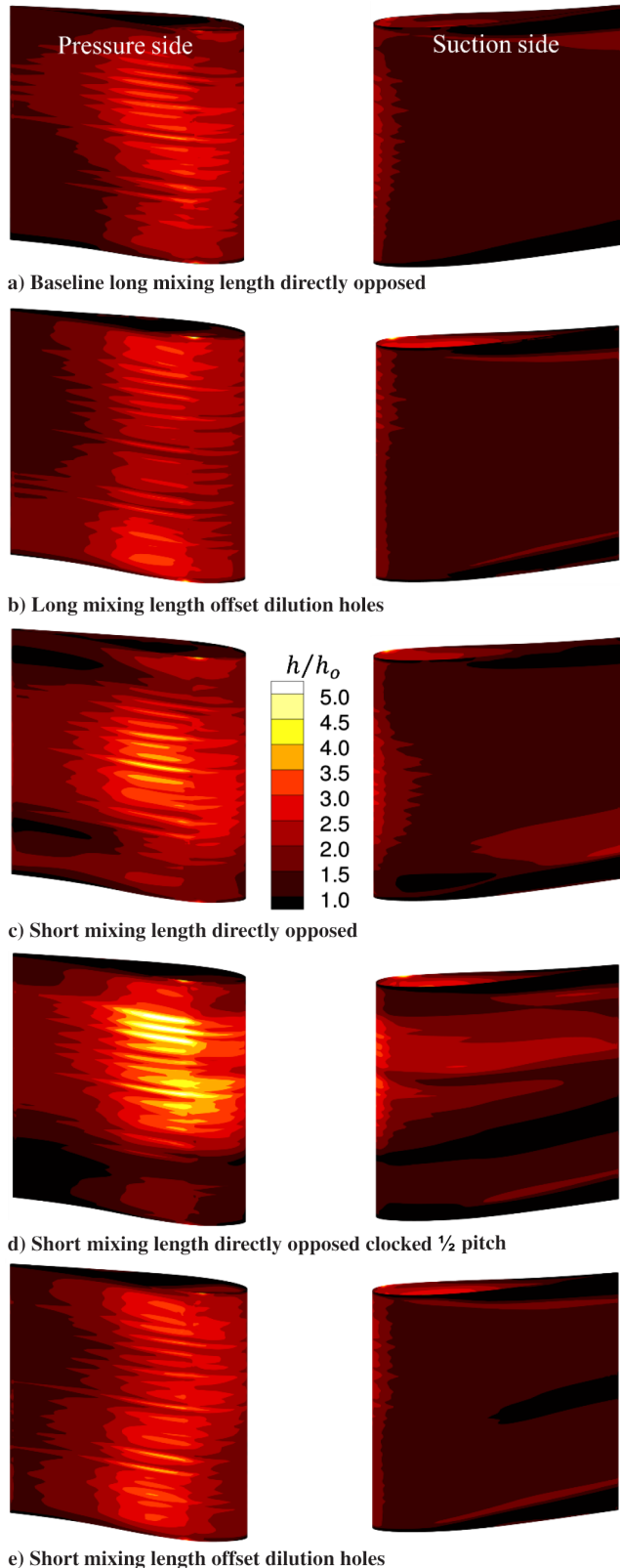


Fig. 12 Nondimensional vane static pressure for the baseline and two short-mixing-length cases.



**Fig. 13 Normalized heat transfer coefficient for each dilution configuration.**

vane for the various dilution configurations in this study. Values of NH greater than zero indicate that the cooling flow reduces heat flux to the vane relative to no cooling, whereas values less than zero indicate increased heat load to the part due to poor cooling and high gas path heat transfer coefficient. In general, the NHFR analysis indicates that there are regions of the vane that may experience increased heat flux, especially near the upper and lower endwalls

where dilution coolant is scarce. Directly opposed cases (Figs. 14a, 14c, and 14d) have lower NHFR (higher heat load) near the endwall than opposed cases, due to the lack of penetration of the dilution jets. For the short mixing length with directly opposed jets (Figs. 14c and 14d), there is a significant cooling benefit at midspan, but a high heat load (low NHFR) near the endwalls, which would result in high thermal stresses in the vane. This is undesirable from a durability standpoint.

Often in turbine design, spatially or circumferentially averaged quantities (velocity, turbulence, temperature) are provided from higher-fidelity unsteady simulations done during combustor design. However, this can mask the complexity of the incoming flow and lead to mispredictions of vane temperature if nonuniformity is not properly understood. Figure 15 shows the mean streamwise velocity (axial direction) through the turbine inlet plane for the various dilution patterns examined. Note that the normalization parameter in Fig. 15 is the mass-average streamwise ( $x$  direction) velocity over the entire plane at this location. The plane is located about 18% of the vane chord upstream of the vane leading edge, and the view in the figures is looking upstream toward the dilution jets. Because of dilution flow mass addition and flow acceleration due to the convergence, the mass-average streamwise velocity at this location is approximately 2.7 times the domain inlet velocity. Note that the turbine inlet plane contours are not perfectly symmetric around the midspan, which would normally be expected for this symmetric combustor geometry. Although the RANS cases had low residuals and were considered converged by the metrics described earlier, the solutions were prone to instability due to the difficulty of the RANS model in capturing the time-average behavior of a naturally unsteady phenomenon.

For the baseline case in Fig. 15a, the turbine inlet velocity shows some nonuniformity associated with the dilution jet trajectories, with two low-velocity regions near the endwall and a high-velocity region near the center. The variation in streamwise velocity can be up to  $\pm 40\%$  relative to the mass-average velocity at that location. In comparison, the offset case with the long mixing length (Fig. 15b) shows a minor improvement in velocity uniformity across the turbine inlet plane. For the short-mixing-length cases in Fig. 15, there are much stronger nonuniformities in the turbine inlet velocity, as might be expected because of the shorter distance between the jets and the turbine inlet. For the directly opposed case that was clocked by half vane pitch (Fig. 15d), the inlet velocity can vary more than  $\pm 60\%$  relative to the average. The effect of clocking the dilution pattern, specifically the low-velocity wake of the large second-row jet, is visible when comparing Fig. 15c versus Fig. 15d. For the offset case with the short mixing length (Fig. 15e), there are regions of very high streamwise velocity near the top and bottom walls, which are the remnants of a dilution jet from one wall impacting the opposite wall. This may not be advantageous for effusion cooling schemes on the combustor walls because the flow could strip off or disturb the effusion.

Figure 16 shows the local turbulence intensity predicted by the RANS model at the turbine inlet plane for the various dilution configurations. Local turbulence intensity was calculated by taking the square root of the local turbulent kinetic energy and normalizing by the same mass-average turbine inlet plane velocity. The baseline case with the directly opposed jets (Fig. 16a) shows turbulence levels of up to 35% at the midspan of the turbine inlet, with low levels of turbulence near the endwall. In contrast, the offset case for the long mixing length (Fig. 16b) has more uniform turbulence distribution, with levels nominally below 30% at midspan but higher turbulence closer to the top and bottom walls. Increased turbulence near the endwalls is likely the primary contributing factor to the increase in normalized vane surface heat transfer coefficients near the endwall in Fig. 13b because the mean flowfield in Figs. 15a and 15b is not much different between the baseline and the long-mixing offset dilution configurations.

The short-mixing-length cases in Fig. 16 have more nonuniform distributions of turbulence intensity, relative to the long-mixing-length cases. For the directly opposed short-mixing-length cases, turbulence levels are highest in the center of the turbine inlet plane, with levels up to 45%. This is much higher than the more commonly assumed level of approximately 20% from prior studies (Barringer et al. [2], Ames et al. [41], Van Fossen and Bunker [42], and Goebel

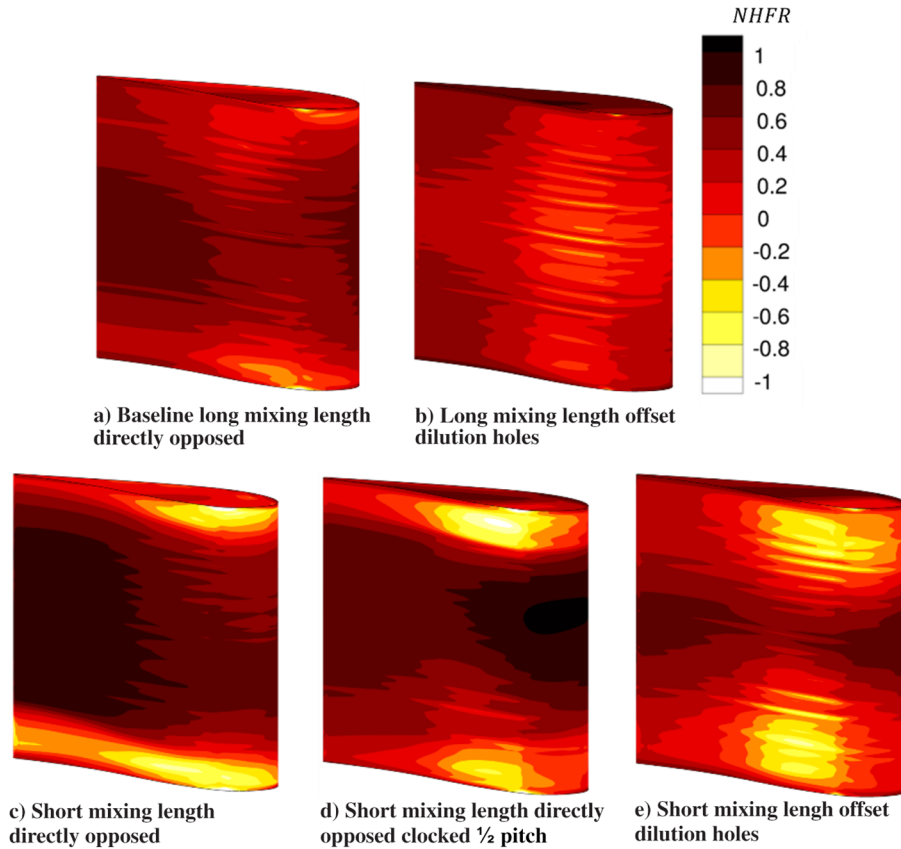


Fig. 14 Net heat flux reduction due to dilution cooling on the vane pressure side.

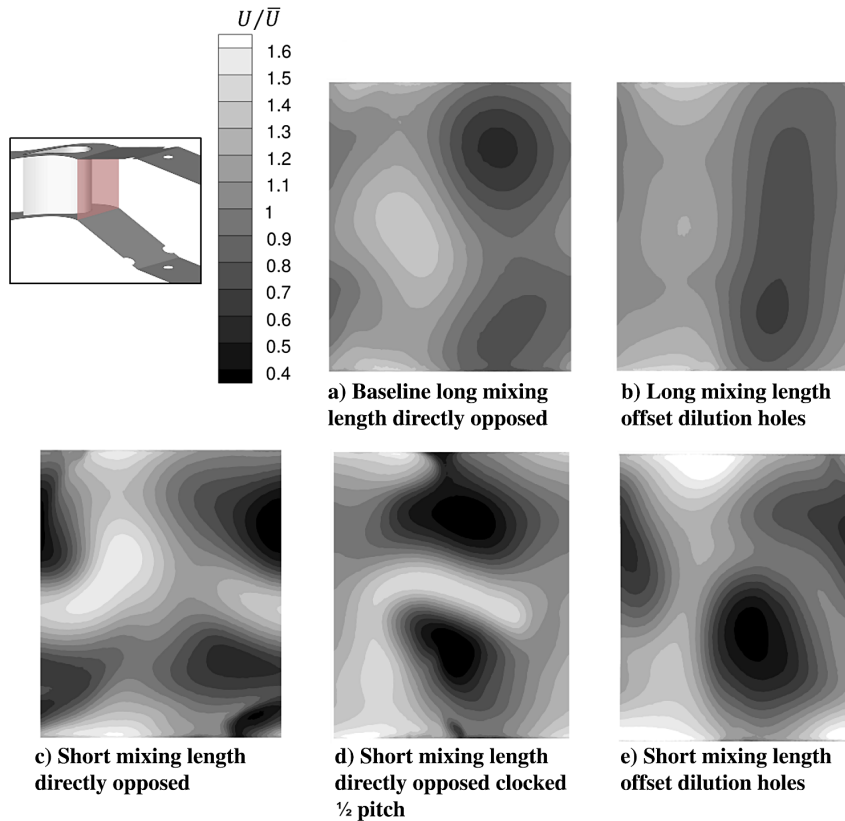


Fig. 15 Mean velocity at the turbine inlet plane (view looking upstream) for the dilution configurations.

et al. [43]), although more recent experimental studies for both RQL-style (Leonetti et al. [44]) and swirl-stabilized combustors (Cha et al. [16]) indicate that turbulence levels may actually exceed 35%. The

offset case for the short mixing length (Fig. 16e) has the highest overall turbulence intensity, with levels of 30% even close to the upper and lower turbine endwalls. Although these high levels of

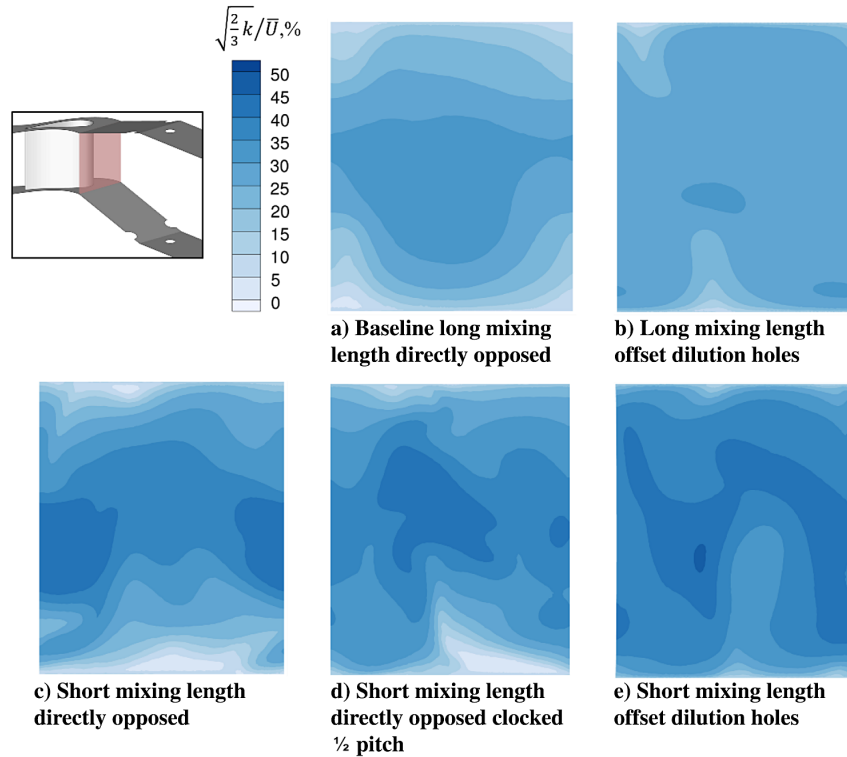


Fig. 16 Local turbulence intensity at the turbine inlet plane for the dilution configurations.

turbulence are beneficial for mixing of combustion products, they do result in high convective heat transfer on the airfoil over a large part of its span (Fig. 13c).

Area-average quantities over the entire vane surface and mass-average quantities over the turbine inlet plane are shown in Table 2. For the vane surface, the directly opposed cases generally result in a greater area-average adiabatic cooling effectiveness than the offset cases, with the baseline configuration having the highest effectiveness. The offset configurations have the lowest average effectiveness for a given development length because the dilution jets do not directly impact the vane. Also shown in Table 2 is the average normalized heat transfer coefficient with dilution flow, where the normalization is the uniform inflow without dilution as described earlier. In all cases, the average normalized heat transfer coefficient on the vane is over 1.5 times larger than for uniform inflow due to the increase in flow turbulence. Long mixing lengths result in slightly lower average heat transfer augmentation, and the offset cases are the lowest overall heat transfer augmentation for a given development length. The highest vane heat transfer augmentation is the short mixing length with directly opposed jets located directly upstream of the vane; Fig. 11 indicates that the wake of the row 2 dilution jets directly impacts on the vane in this configuration.

Considering the turbine inlet plane mass-average results in Table 2, the offset cases have a cooler nondimensional temperature

(higher  $\theta$ ) entering the turbine than the directly opposed cases, and the shorter-mixing-length cases have generally an equal or higher  $\theta$  than the long-mixing-length cases. This is due to the close proximity of the coolant flow to the turbine inlet plane in the short-mixing-length configurations producing cooler “cold regions” and warmer “hot regions” than the more fully mixed cases with a longer development length. The mass-average values of turbulence intensity, ranging from 24% for long development length to 43% for short development length, are somewhat higher than the commonly assumed 20% [2,30,31].

The local effect of the different combustor geometries on vane surface temperature is plotted along the vane leading edge in Fig. 17a. This figure shows the adiabatic effectiveness along the span of the vane leading edge, from lower ( $z/S = 0$ ) to upper ( $z/S = 1$ ) endwalls. Though all of the configurations have approximately the same midspan performance, the endwall thermal loading is very different. The offset configurations have a lower temperature (higher  $\eta$ ) near the endwall than their directly opposed counterparts. In the short-mixing-length cases, the directly opposed and clocked configuration has a higher effectiveness at midspan than the short-mixing-length offset case except near the endwalls, due to the larger quantity of dilution air impinging directly on the leading edge. The long-mixing-length offset case has both the lowest endwall temperature (highest effectiveness) and the most uniform spanwise profile, which is generally why this configuration is most preferred in modern engine design.

Figure 17b is a plot of adiabatic effectiveness around the vane surface at 50% span (midspan). The average value at midspan for each configuration is approximately the same, with small differences between the pressure side and suction side. It is clear from this figure that longer mixing length results in a more uniform effectiveness profile around the vane. In cooling performance, the clocking of the short-mixing-length case results in a similar profile to the short-mixing-length offset case, with more cooling of the leading edge and less of the trailing edge, a result of the large amount of cooling air aligned with the leading edge very close to the vane.

The normalized heat transfer around the vane at 50% span is plotted in Fig. 18, where  $s/C$  is the surface distance along the vane from the leading-edge stagnation normalized by the vane true chord, and positive  $s/C$  is toward the suction side. To generate this plot, the

Table 2 Average values for the vane surface and turbine inlet plane

Case	Vane surface area average		Turbine inlet plane mass average	
	$\eta$	$h/h_0$	$\theta$	Turbulence intensity, %
Baseline, long mixing length	0.41	1.59	0.35	24
Long mixing length, offset	0.37	1.58	0.36	28
Short mixing length, directly opposed	0.40	1.65	0.35	33
Short mixing length, offset	0.36	1.63	0.38	42
Short mixing length, directly opposed, clocked	0.38	1.75	0.37	43

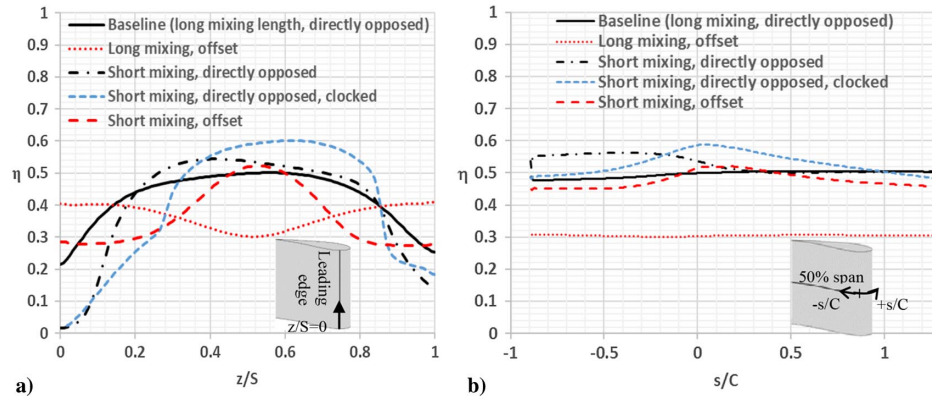


Fig. 17 Vane nondimensional temperature a) along the leading edge ( $Y = 0$ ), and b) around the vane at 50% span ( $Z = 0.273$  m).

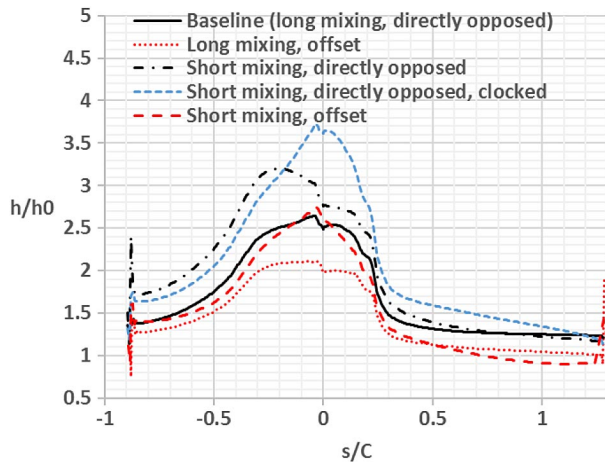


Fig. 18 Normalized heat transfer coefficient for each case at 50% span.

surface heat transfer at a given  $s/C$  was averaged over the middle 10% of the vane span ( $\pm 5\%$  around midspan) to minimize the effects of the streakiness of the contours. The majority of the heat transfer coefficient augmentation occurs on the leading edge and pressure side of the vane, with augmentation between two to over three times that of the clean inflow. Also, the long-mixing-length cases exhibit lower augmentation than the corresponding short-mixing-length cases, and high augmentation regions on the vane leading edge generally track with the dilution jet trajectory (Fig. 11). The greatest augmentation factors occur for the cases with the jets that impinge directly on the vane (short mixing length directly opposed, and short mixing length directly opposed and clocked).

### B. Comparison of Steady Reynolds-Averaged Navier–Stokes to Delayed Detached-Eddy Simulation

The time-average result (total of nine flow-through time samples, or 5.4 s) from the nominal-grid DDES solution of the baseline case is shown in Fig. 19. It is immediately apparent by comparing the

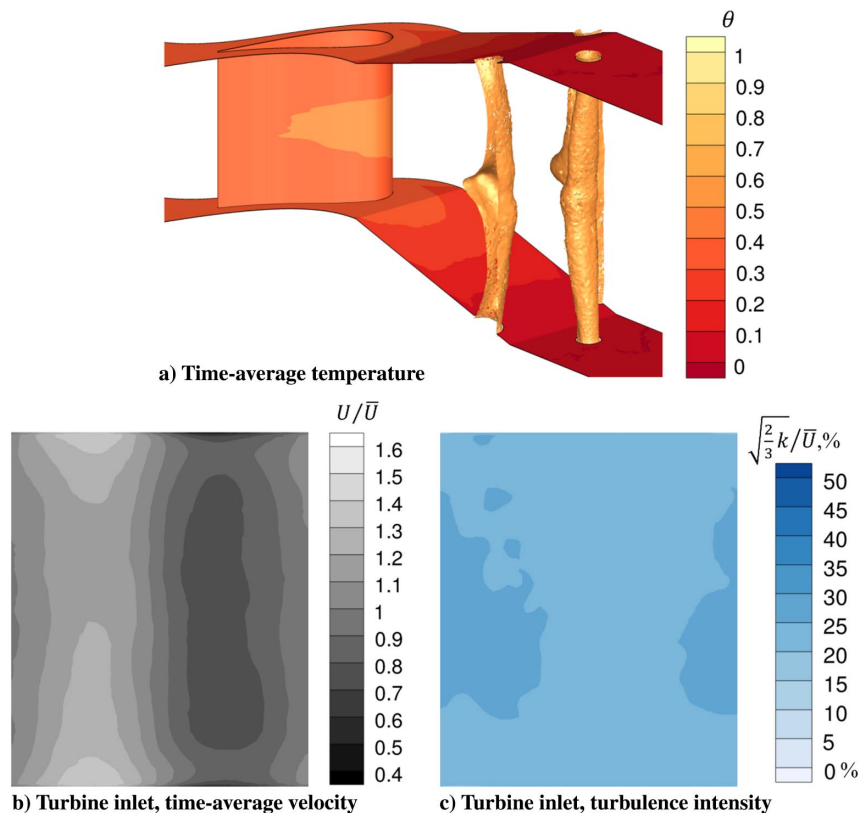


Fig. 19 Time-average results for the DDES solution of the baseline geometry on the nominal grid of 12 million cells.

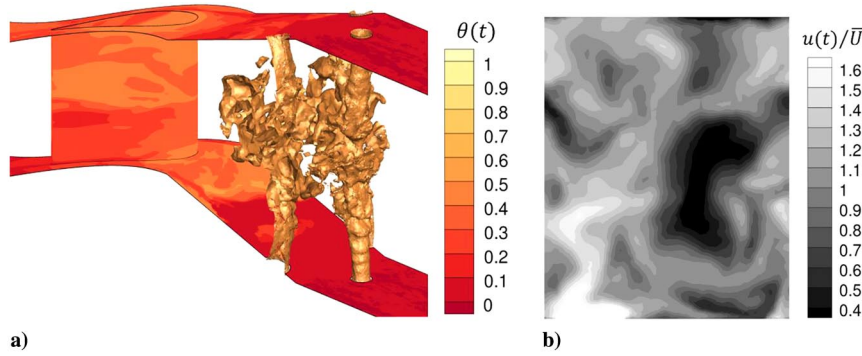


Fig. 20 Representations of a) instantaneous temperature (isosurfaces at  $\theta = 0.55$ ), and b) instantaneous streamwise velocity at the turbine inlet plane.

isosurfaces of nondimensional temperature between the baseline in Figs. 11a and 19a that the dilution jets do not retain coherency as far downstream in the DDES time-average result. This is due to the more accurate prediction of mixing in the time-resolved DDES case, as expected. Another important difference is the endwall temperature in the vane passage, which is lower for the DDES versus the RANS case due to increased mixing of the dilution flow.

At the turbine inlet plane, the mean streamwise velocity is more uniform in the spanwise (vertical) direction for the DDES (Fig. 19b) versus RANS (Fig. 15a), again due to the better mixing, but there is still a distinct difference in velocity between the right and left sides of the plane. This is due to the pressure field of the vane at this location, which slows down the approaching fluid on the right (pressure side of the vane) and increases it on the left (accelerating around the suction side of the vane). The turbulence intensity is also more uniform and lower in magnitude near the midspan ( $\sim 25\%$ ) for the DDES simulation (Fig. 19c) relative to the RANS case (Fig. 16a). Interestingly, the turbulence intensity is predicted to be higher near the upper and lower endwalls, in the DDES case. Thus, a RANS simulation of this dilution configuration would perhaps underpredict the level of heat transfer enhancement on the turbine endwalls.

The instantaneous behavior of the flow from the DDES case is shown in Fig. 20, for the surface temperature and the turbine inlet plane. The rollup of the first-row dilution jet shear layer is apparent in the isosurfaces in Fig. 20a. Also, a fairly significant hotspot is shown on the vane pressure side surface near the trailing edge. However, because of the thermal capacitance of the metal in a turbine vane in the engine, this instantaneous increase in adiabatic wall temperature would not likely have an impact on the operational metal temperature; Fig. 19a indicates only a modest difference in time-average temperature over the vane surface. At the turbine inlet plane, Fig. 20b indicates a wide range of turbulent structures entering the turbine, with instantaneous velocities that are up to  $\pm 60\%$  of the time- and space-average value of  $\bar{U} = 4.4$  m/s.

Because the temperature fluctuations are also temporally resolved in the DDES simulation, it is interesting to understand where the fluctuations are the largest on the surfaces of interest (combustor walls, turbine airfoil). Figure 21 shows a semitransparent isosurface of instantaneous  $\theta$  at a level of 0.4 as well as contours of the rms of

fluctuations in surface temperature. Here, it is apparent that the region that would be most highly distressed by fluctuating temperatures is the combustor convergence immediately downstream of the dilution jets. The vane centerline shows the lowest fluctuations in surface temperature, although the upper and lower vane passage endwalls are slightly higher. These are regions of higher uncertainty in local adiabatic wall temperature and could be accounted for in a statistically based durability design.

Also of interest to turbine design is the correctness of representing the inlet turbulence condition via a single quantity, namely the turbulent kinetic energy  $k$ . Figure 22 shows the rms of the streamwise ( $u$ ), pitchwise ( $v$ ), and spanwise ( $w$ ) velocity components from the DDES model at the turbine inlet plane. If the components are all equivalent, the turbulence field would be isotropic and could be represented by a single quantity. However, this does not appear to be the case for this baseline configuration. In particular, the spanwise velocity fluctuations are about 30% larger than the streamwise fluctuations at the sides of the turbine inlet plane. The primary source of the turbulence is from the shear layers in the dilution jets, which generate high  $w$ -fluctuations due to the jet injection direction, and there is insufficient distance for the turbulence to become isotropic. Figure 23 shows an axial slice that intersects the second-row dilution hole. Contours of the three turbulence components are plotted to show how the turbulence develops at dilution injection and propagates downstream. It is clear that a large part of the turbulence is generated in both the shear layers of the jet as well as the interaction between opposing jets. The anisotropy of the turbulence at the turbine inlet plane is largely due to the different strengths of the various components at the dilution injection as well as insufficient distance downstream of dilution to reach isotropy. Note that the turbulence is also not isotropic near the upper and lower endwalls, which would impact the ability of a RANS model to properly predict that effect on surface temperature.

### C. Effect of Delayed Detached-Eddy Simulation Grid Refinement

As described earlier, the DDES grid was refined using local adaptation based on the ratio of the cube root of cell volume to the local Kolmogorov length scale. The impact of this refinement was primarily in the initial dilution zone, but it was not clear whether this would impact the convection and dissipation of turbulent scales entering the turbine. Figure 24 shows the time-average results for the refined DDES case. Note that, because of computational resource limitations, the refined DDES has not been sampled for an equivalent amount of time, though both models demonstrated statistical stationarity.

The isosurfaces of  $\theta$  are similar in terms of jet trajectory between Figs. 19a and 24a, although the refined DDES predicts that the time-average jet profile from the second row of dilution will persist farther downstream. This is likely because the refined model is better capturing the range of scales of the turbulent dissipation of the jets, whereas the coarseness of the nominal DDES grid results in additional numerical dissipation. The effect on the vane surface temperature is minor, with slightly lower temperature (higher  $\eta$ ) predicted by the refined DDES case in the midspan. The time-average turbine inlet plane quantities in Figs. 24b–24f compare fairly well to

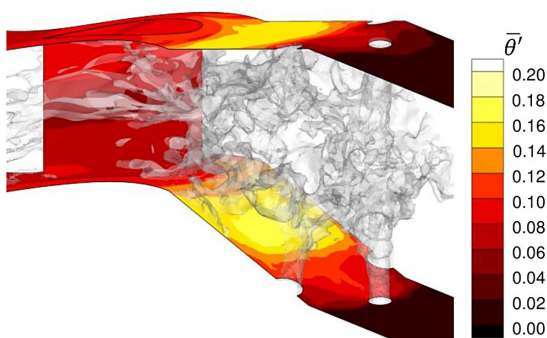


Fig. 21 Isosurfaces (semitransparent) of instantaneous  $\theta = 0.4$ , with surface contours of rms of  $\theta$ .

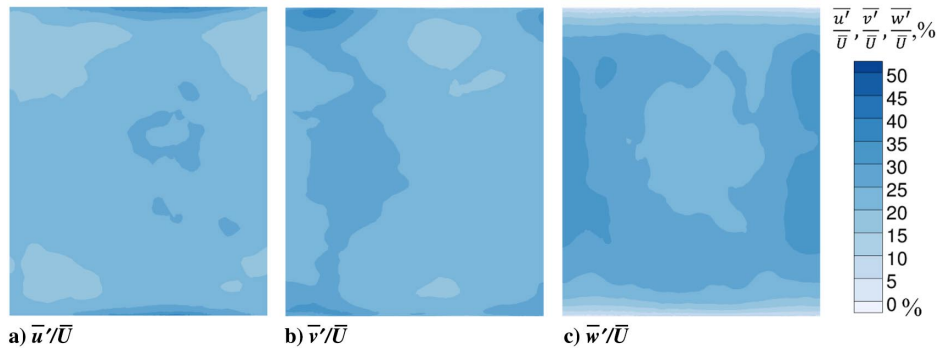


Fig. 22 Streamwise ( $u$ ), pitchwise ( $v$ ), and spanwise ( $w$ ) velocity fluctuations at the turbine inlet plane.

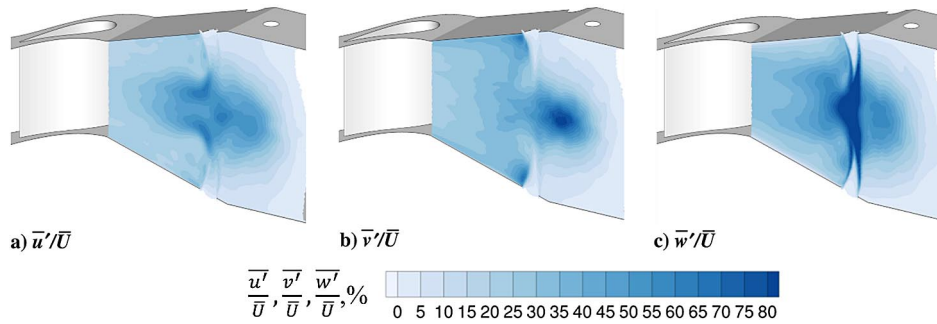


Fig. 23 Streamwise ( $u$ ), pitchwise ( $v$ ), and spanwise ( $w$ ) velocity fluctuations on an  $x$ - $y$  plane intersecting the second dilution row.

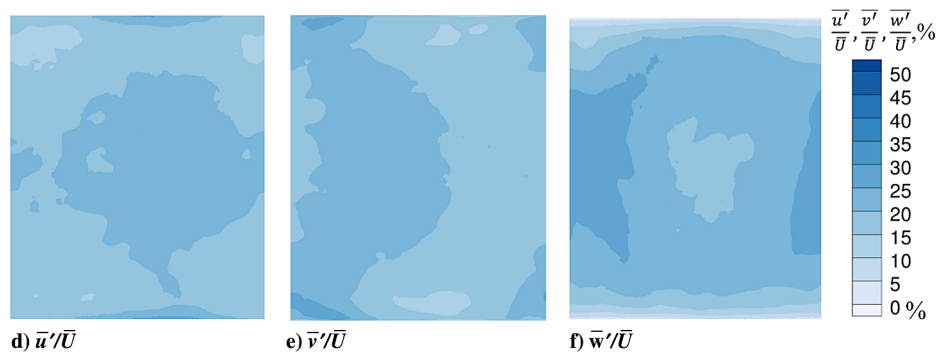
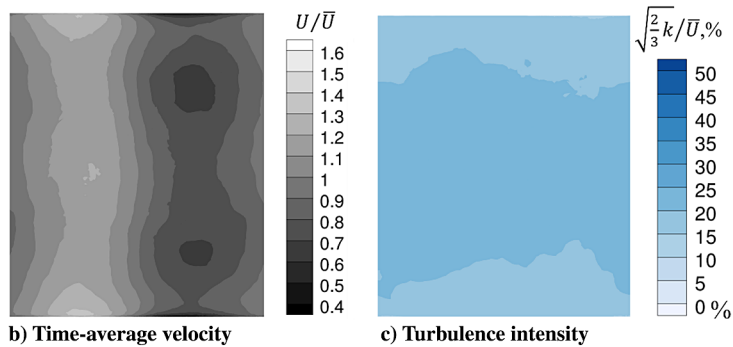
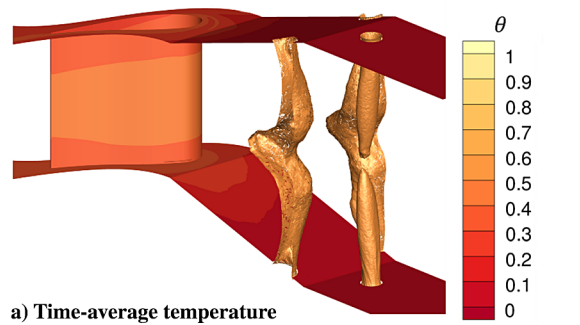


Fig. 24 Time-average temperature and isosurface (Fig. 24a) and turbine inlet plane results (Figs. 24b–24f) for the refined DDES grid.

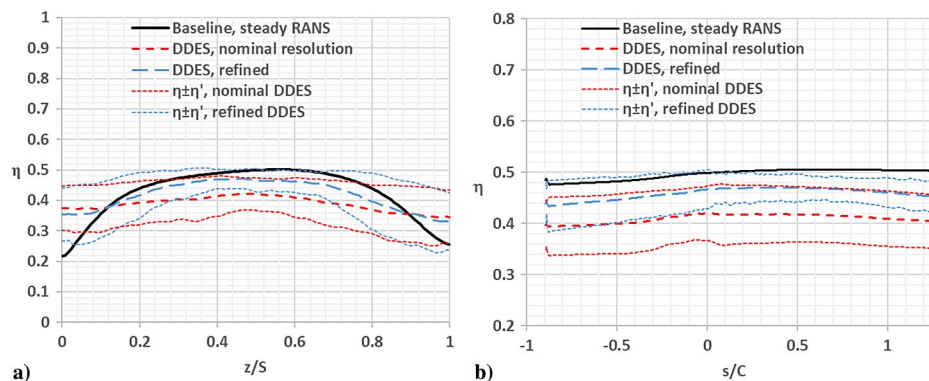


Fig. 25 Representations of a) vane leading-edge temperature, and b) vane midspan temperature, for RANS, DDES, and refined DDES.

the nominal DDES results in Figs. 19b, 19c, and 22, although the refined DDES predicts slightly lower turbulence levels. This is the result of increased mixing predicted by the refined DDES.

The effect of turbulent mixing on the vane surface temperature is shown quantitatively along the vane leading edge in Fig. 25 for the RANS, DDES, and refined DDES cases. The “envelope” of temperature variation from the two DDES cases is also plotted as a thin dotted line with the same color as the mean value for that case, where the variation is defined here as the time-average value plus or minus the rms of the value at that location. Although there is some difference in the mean value between the two DDES cases, both predict more uniform vane temperature over the vane span than the RANS case of the same geometry, with a significantly higher mean effectiveness near the endwalls. The DDES cases also indicate lower temporal variation in vane surface temperature near the midspan but higher variation near the endwalls, which could translate to higher vane temperature confidence at midspan versus the endwall for a stochastic design methodology. Interestingly, the RANS prediction does tend to fall within the variation from the DDES cases, but this result suggests that a cooling design based solely on a RANS prediction of the vane would tend to overestimate the cooling required at the endwalls.

The predicted vane midspan surface temperature is plotted along the normalized vane surface distance in Fig. 25b. All predictions indicate a relatively uniform surface temperature around the vane for this long development length, with the RANS predicting the coolest vane temperature (highest  $\eta$ ). There is a slight increase in mean vane effectiveness and a somewhat narrower variation around the mean for the refined DDES versus the nominal DDES grid resolution. As suggested earlier, the better spatial resolution of the near-jet structures may contribute to an improved prediction of turbulent transport and less numerical dissipation.

## VI. Conclusions

A computational study of a combustor–turbine configuration with upstream dilution was performed using steady RANS and time-dependent DDES calculations. The effect of dilution hole position on the downstream turbine vane was investigated using steady RANS. A particular focus of this part of the study was consideration of the impact of the dilution flow variation on vane surface heat transfer. The baseline configuration was also investigated using DDES, to resolve turbulent scales of the large dilution jets, and compared to the RANS baseline. Finally, a refined DDES model was run to determine if turbine inlet and vane surface quantities were impacted by increased resolution in the dilution jet region.

The steady RANS models indicated better uniformity but higher overall turbulence levels for dilution jet configurations where the upper and lower jets were offset, relative to jets with centerlines directly opposed to each other. Shifting the dilution jets 50% closer to the vane resulted in increased inlet flow nonuniformity and very high turbulence levels, as well as creating more significant temperature gradients on the vane and endwall surfaces downstream of the jets. It appears that dilution jets located close to the vane might be useful

to augment vane cooling, but surface convective heat transfer coefficients increase significantly, and likely the high unsteadiness of the incoming flow would negatively impact vane surface film cooling. In particular, the leading edge and pressure side of the vane could experience heat transfer coefficient augmentation up to three times larger than for a clean inlet flow. Also, the high freestream turbulence leads to significant increases in heat flux (negative net heat flux reduction) near the endwalls where little dilution coolant is present. Overall, this work indicates that a shorter combustor design should carefully consider the interaction of the dilution flow with the downstream vane.

As expected, the DDES scale-resolving simulations predicted more mixing of the dilution jet than the steady RANS result, so that the turbine vane and endwall surface temperatures were more uniform. Turbine inlet velocity and turbulence level were also more uniform, although turbulence levels were still high ( $\sim 25\%$ ). Evaluation of the individual fluctuating velocity components indicates that the incoming turbulence is anisotropic, particularly closer to the vane endwall surfaces, which cannot be captured by a RANS approach. The effect of the turbulence anisotropy and its propagation through the turbine should be investigated in more detail. Refinement of the DDES grid around the initial injection of the dilution jets appeared to have a minor impact on the predicted turbine inlet quantities, although there was some slight difference in the vane surface temperature.

This study indicates the potential pitfalls of close interaction between the combustor and vane for short combustor lengths as well as how the vane cooling scheme may need to account for significant thermal gradients. Also, it is important to resolve major turbulent structures and their propagation to accurately simulate conditions for the first vane for cooling design. Future work should incorporate reacting flow, investigate the predicted turbulent length scales, and determine how nonuniform inlet conditions could be better incorporated in a RANS approach to improve accuracy of turbine vane temperature predictions without sacrificing run time, which is currently prohibitive for some scale-resolving methods. Certainly, high-resolution experimental data at the turbine interface and on the vane surface are also needed to verify computational models.

## Acknowledgments

The authors would like to thank the Pennsylvania State University College of Engineering’s undergraduate research experience program for providing partial support for the first author. Computations for this research were performed on Pennsylvania State University’s Institute for CyberScience Advanced CyberInfrastructure.

## References

- [1] Fric, T. F., and Roshko, A., “Vortical Structure in the Wake of a Transverse Jet,” *Journal of Fluid Mechanics*, Vol. 279, Nov. 1994, pp. 1–47.  
doi:10.1017/S0022112094003800

- [2] Barringer, M. D., Richard, O. T., Walter, J. P., Stitzel, S. M., and Thole, K. A., "Flow Field Simulations of a Gas Turbine Combustor," *Journal of Turbomachinery*, Vol. 124, No. 3, 2002, pp. 508–516.  
doi:10.1115/1.1475742
- [3] Epstein, A. H., "Aeropropulsion for Commercial Aviation in the Twenty-First Century and Research Directions Needed," *AIAA Journal*, Vol. 52, No. 5, 2014, pp. 901–911.  
doi:10.2514/1.J052713
- [4] McKinney, R., Cheung, A., Sowa, W., and Sepulveda, D., "The Pratt & Whitney Talon X Low Emissions Combustor: Revolutionary Results with Evolutionary Technology," *45th AIAA Aerospace Sciences Meeting and Exhibit*, AIAA Paper 2007-0386, 2007.  
doi:10.2514/6.2007-386
- [5] Vakil, S. S., and Thole, K. A., "Flow and Thermal Field Measurements in a Combustor Simulator Relevant to a Gas Turbine Aeroengine," *Journal of Engineering for Gas Turbines and Power*, Vol. 127, No. 2, 2005, pp. 257–267.  
doi:10.1115/1.1806455
- [6] Holdeman, J. D., and Walker, R., "Mixing of a Row of Jets with a Confined Crossflow," *AIAA Journal*, Vol. 15, No. 2, 1977, pp. 243–249.  
doi:10.2514/3.60622
- [7] Holdeman, J. D., Srinivasan, R., and Berenfeld, A., "Experiments in Dilution Jet Mixing," *AIAA Journal*, Vol. 22, No. 10, 1984, pp. 1436–1443.  
doi:10.2514/3.48582
- [8] Stevens, S. J., and Carrotte, J. F., "Experimental Studies of Combustor Dilution Zone Aerodynamics. I—Mean Flowfields," *Journal of Propulsion and Power*, Vol. 6, No. 3, 1990, pp. 297–304.  
doi:10.2514/3.25434
- [9] Stevens, S. J., and Carrotte, J. F., "Experimental Studies of Combustor Dilution Zone Aerodynamics. II—Jet Development," *Journal of Propulsion and Power*, Vol. 6, No. 4, 1990, pp. 504–511.  
doi:10.2514/3.25463
- [10] Dai, W., Zhang, Y., Lin, Y., Yang, Q., and Zhang, C., "Influence of the Arrangement of Dilution Holes for Dilution Mixing in a Three-Injector Reverse Flow Combustor," *ASME Turbo Expo 2014: Turbine Technical Conference and Exposition*, ASME Paper GT2014-25235, New York, 2014.  
doi:10.1115/gt2014-25235
- [11] Cha, C. M., Hong, S., Ireland, P. T., Denman, P., and Savarianandam, V., "Experimental and Numerical Investigation of Combustor–Turbine Interaction Using an Isothermal, Nonreacting Tracer," *Journal of Engineering for Gas Turbines and Power*, Vol. 134, No. 8, 2012, Paper 081501.  
doi:10.1115/1.4005815
- [12] di Mare, F., Jones, W. P., and Menzies, K. R., "Large Eddy Simulation of a Model Gas Turbine Combustor," *Combustion and Flame*, Vol. 137, No. 3, 2004, pp. 278–294.  
doi:10.1016/j.combustflame.2004.01.008
- [13] Moin, P., and Apte, S. V., "Large-Eddy Simulation of Realistic Gas Turbine Combustors," *AIAA Journal*, Vol. 44, No. 4, 2006, pp. 698–708.  
doi:10.2514/1.14606
- [14] Patil, S., and Tafti, D., "Large-Eddy Simulation of Flow and Convective Heat Transfer in a Gas Turbine Can Combustor with Synthetic Inlet Turbulence," *Journal of Engineering for Gas Turbines and Power*, Vol. 134, No. 7, 2012, Paper 071503.  
doi:10.1115/1.4006081
- [15] Boudier, G., Gicquel, L. Y. M., Poinso, T., Bissières, D., and Bérat, C., "Comparison of LES, RANS and Experiments in an Aeronautical Gas Turbine Combustion Chamber," *Proceedings of the Combustion Institute*, Vol. 31, No. 2, 2007, pp. 3075–3082.  
doi:10.1016/j.proci.2006.07.067
- [16] Cha, C. M., Ireland, P. T., Denman, P. A., and Savarianandam, V., "Turbulence Levels Are High at the Combustor–Turbine Interface," *ASME Turbo Expo 2012: Turbine Technical Conference and Exposition*, ASME Paper GT2012-69130, New York, 2012.  
doi:10.1115/GT2012-69130
- [17] Salvadori, S., Riccio, G., Insinna, M., and Martelli, F., "Analysis of Combustor/Vane Interaction with Decoupled and Loosely Coupled Approaches," *ASME Turbo Expo 2012: Turbine Technical Conference and Exposition*, ASME Paper GT2012-69038, New York, 2012.  
doi:10.1115/GT2012-69038
- [18] Insinna, M., Salvadori, S., and Martelli, F., "Simulation of Combustor/NGV Interaction Using Coupled RANS Solvers: Validation and Application to a Realistic Test Case," *ASME Turbo Expo: Power for Land, Sea, and Air*, No. 45622, 2014, Paper V02CT38A010.  
doi:10.1115/GT2014-25433
- [19] Medic, G., Kalitzin, G., You, D., van der Weide, E., Alonso, J., and Pitsch, H., "Integrated RANS/LES Computations of an Entire Gas Turbine Jet Engine," *45th AIAA Aerospace Sciences Meeting and Exhibit*, AIAA Paper 2007-1117, 2008.  
doi:10.2514/6.2007-1117
- [20] Klapdor, E., Di Mare, F., Kollmann, W., and Janicka, J., "A Compressible Pressure-Based Solution Algorithm for Gas Turbine Combustion Chambers Using the PDF/FGM Model," *Flow, Turbulence and Combustion*, Vol. 91, No. 2, 2013, pp. 209–247.  
doi:10.1007/s10494-013-9451-2
- [21] Andreini, A., Bacci, T., Insinna, M., Mazzei, L., and Salvadori, S., "Hybrid RANS-LES Modeling of the Aerothermal Field in an Annular Hot Streak Generator for the Study of Combustor–Turbine Interaction," *Journal of Engineering for Gas Turbines and Power*, Vol. 139, No. 2, 2017, Paper 021508.  
doi:10.1115/1.4034358
- [22] Ames, F. E., "The Influence of Large-Scale High-Intensity Turbulence on Vane Heat Transfer," *Journal of Turbomachinery*, Vol. 119, No. 1, 1997, pp. 23–30.  
doi:10.1115/1.2841007
- [23] Ames, F. E., Argenziano, M., and Wang, C., "Measurement and Prediction of Heat Transfer Distributions on an Aft-Loaded Vane Subjected to the Influence of Catalytic and Dry Low Nox Combustor Turbulence," *Journal of Turbomachinery*, Vol. 126, No. 1, 2004, pp. 139–149.  
doi:10.1115/1.1645867
- [24] Ames, F. E., Wang, C., and Barbot, P. A., "Measurement and Prediction of the Influence of Catalytic and Dry Low Nox Combustor Turbulence on Vane Surface Heat Transfer," *Journal of Turbomachinery*, Vol. 125, No. 2, 2003, pp. 221–231.  
doi:10.1115/1.1559898
- [25] Radomsky, R. W., and Thole, K. A., "Flowfield Measurements for a Highly Turbulent Flow in a Stator Vane Passage," *Journal of Turbomachinery*, Vol. 122, No. 2, 2000, pp. 255–262.  
doi:10.1115/1.555442
- [26] Barringer, M. D., Polanka, M. D., and Thole, K. A., "Effects of Combustor Exit Profiles on Vane Aerodynamic Loading and Heat Transfer in a High Pressure Turbine," *Journal of Turbomachinery*, Vol. 131, No. 2, 2009, Paper 021008.  
doi:10.1115/1.2950051
- [27] Povey, T., and Qureshi, I., "Developments in Hot-Streak Simulators for Turbine Testing," *Journal of Turbomachinery*, Vol. 131, No. 3, 2009, Paper 031009.  
doi:10.1115/1.2987240
- [28] Basol, A. M., Kalfas, A. I., Abhari, R. S., and Kai, R., "Integrated Combustor Turbine Design for Improved Aerothermal Performance: Effect of Dilution Air Control," *Journal of Engineering for Gas Turbines and Power*, Vol. 134, No. 9, 2012, Paper 091501.  
doi:10.1115/1.4006671
- [29] Griffini, D., Insinna, M., Salvadori, S., and Martelli, F., "Clocking Effects of Inlet Nonuniformities in a Fully Cooled High-Pressure Vane: A Conjugate Heat Transfer Analysis," *Journal of Turbomachinery*, Vol. 138, No. 2, 2015, Paper 021006.  
doi:10.1115/1.4031864
- [30] Kang, M. B., Kohli, A., and Thole, K. A., "Heat Transfer and Flowfield Measurements in the Leading Edge Region of a Stator Vane Endwall," *Journal of Turbomachinery*, Vol. 121, No. 3, 1999, pp. 558–568.  
doi:10.1115/1.2841351
- [31] Menter, F. R., "Two-Equation Eddy-Viscosity Turbulence Models for Engineering Applications," *AIAA Journal*, Vol. 32, No. 8, 1994, pp. 1598–1605.  
doi:10.2514/3.12149
- [32] *Ansys Fluent: Theory Guide*, v16.1 ed., ANSYS, Canonsburg, PA, [https://www.sharcnet.ca/Software/Ansys/16.2.3/en-us/help/flu\\_th/flu\\_th.html](https://www.sharcnet.ca/Software/Ansys/16.2.3/en-us/help/flu_th/flu_th.html).
- [33] Gritskevich, M. S., Garbaruk, A. V., Schütze, J., and Menter, F. R., "Development of DDES and IDDES Formulations for the  $K - \omega$  Shear Stress Transport Model," *Flow, Turbulence and Combustion*, Vol. 88, No. 3, 2012, pp. 431–449.  
doi:10.1007/s10494-011-9378-4
- [34] Agarwal, K. K., Konakalla, S. R., and Selvan, S., "On Meshing Guidelines for Large Eddy Simulations of Gas Turbine Combustors," *ASME Turbo Expo 2014: Turbine Technical Conference and Exposition*, ASME Paper GT2014-26077, New York, 2014.  
doi:10.1115/gt2014-26077
- [35] Lefebvre, A. H., and Ballal, D. R., *Gas Turbine Combustion*, CRC Press, Ann Arbor, MI, 2010.
- [36] Stitzel, S., and Thole, K. A., "Flow Field Computations of Combustor–Turbine Interactions Relevant to a Gas Turbine Engine," *Journal of Turbomachinery*, Vol. 126, No. 1, 2004, pp. 122–129.  
doi:10.1115/1.1625691

- [37] Wagner, J. A., Grib, S. W., Renfro, M. W., and Cetegen, B. M., "Flowfield Measurements and Flame Stabilization of a Premixed Reacting Jet in Vitiated Crossflow," *Combustion and Flame*, Vol. 162, No. 10, 2015, pp. 3711–3727.  
doi:10.1016/j.combustflame.2015.07.010
- [38] Sullivan, R., Wilde, B., Noble, D. R., Seitzman, J. M., and Lieuwen, T. C., "Time-Averaged Characteristics of a Reacting Fuel Jet in Vitiated Cross-Flow," *Combustion and Flame*, Vol. 161, No. 7, 2014, pp. 1792–1803.  
doi:10.1016/j.combustflame.2013.12.022
- [39] Winoto, S., and Crane, R., "Vortex Structure in Laminar Boundary Layers on a Concave Wall," *International Journal of Heat and Fluid Flow*, Vol. 2, No. 4, 1980, pp. 221–231.  
doi:10.1016/0142-727X(80)90016-8
- [40] Sen, B., Schmidt, D. L., and Bogard, D. G., "Film Cooling with Compound Angle Holes: Heat Transfer," *Journal of Turbomachinery*, Vol. 118, No. 4, 1996, pp. 800–806.  
doi:10.1115/1.2840937
- [41] Ames, F. E., Barbot, P. A., and Wang, C., "Effects of Aeroderivative Combustor Turbulence on Endwall Heat Transfer Distributions Acquired in a Linear Vane Cascade," *Journal of Turbomachinery*, Vol. 125, No. 2, 2003, pp. 210–220.  
doi:10.1115/1.1559897
- [42] Van Fossen, G. J., and Bunker, R. S., "Augmentation of Stagnation Region Heat Transfer due to Turbulence from a DLN Can Combustor," *Journal of Turbomachinery*, Vol. 123, No. 1, 2001, pp. 140–146.  
doi:10.1115/1.1330270
- [43] Goebel, S., Abuaf, N., Lovett, J., and Lee, C.-P., "Measurements of Combustor Velocity and Turbulence Profiles," *ASME 1993 International Gas Turbine and Aeroengine Congress and Exposition*, ASME, New York, 1993.  
doi:10.1115/93-gt-228
- [44] Leonetti, M., Lynch, S., O'Connor, J., and Bradshaw, S., "Combustor Dilution Hole Placement and Its Effect on the Turbine Inlet Flowfield," *Journal of Propulsion and Power*, Vol. 33, No. 3, 2017, pp. 750–763.  
doi:10.2514/1.B36308

C. S. Tan  
Associate Editor